Synthesis and Characterization of Functionalized Nanomaterials: Heterogeneous Palladium Catalyst and Lithium-Doped Graphene Oxide

A Dissertation Presented for the
Doctor of Philosophy
Degree
The University of Tennessee, Knoxville

Benjamin Evan Estes
August 2012

ACKNOWLEDGEMENTS

I would first like to thank my adviser, Professor John Z. Larese, for his guidance and patience throughout my graduate studies. He believed in me even when I didn't believe in myself and has taught me as much about life as about chemistry. His devotion to his research group, to science, and to his family will continue to serve as guideposts for how to lead a successful career and balanced life.

I would also like to thank my parents, Gary and Patricia, for their love, for always providing a wonderful home, and for being great role models. Thank you both for instilling the importance of education and hard work, and for providing me with the opportunity to pursue my goals.

I would like to thank my previous research advisers: at Eastern Kentucky University, C. Frank Shaw, III, and at the University of Tennessee, John F. C. Turner. Despite a busy schedule as department head, lecturer, and active researcher, Dr. Shaw found time to mentor me, direct me toward a major in chemistry, and then onto graduate studies. Dr. Turner gave me an in-depth training in organometallic chemistry, but more importantly, shared his passion for science and education. He continues to be a source of inspiration. These two men gave their time, energy, and precious research funds to foster in me and countless others an interest in science. I am very lucky to have crossed paths with these two fine educators and scientists.

I would like to thank my collaborators at Oak Ridge National Laboratory: Andrew Lupini, Craig Bridges and Harry Meyer; as well as Luke Daemen at Los Alamos National Laboratory. By gaining access to their expertise and the national laboratory facilities, my education and research capabilities have been enriched.

I am also very lucky to have worked with the many wonderful students with whom I've shared a laboratory throughout my years of study. They lent me a hand while working at the lab bench, lent me an ear into which I could vent my frustrations in this sometimes maddening field of study, and shared their talents and expertise on a daily basis. There are many people among this list that will surely be my lifelong friends, and many who will no doubt have distinguished careers in chemistry: Ashley McNiel, Sylvia McLain, Megan Bragg, Cara Nygren, Andy Colvin, Jamie Molaison, Mike Blanchard, Brad O'Dell, Sami Chanaa, Peter Yaron, Hangning Chen, Andi Barbour, Paige Landry, Lillian Frazier, Michael Felty, George Thomas, Andy Hicks, Nathaniel Bass, George Rouvelas, and Sourav Adak. Thank you all.

I would like to thank the University of Tennessee and the many members of the Department of Chemistry staff that have often bent over backwards to see that I finished this degree program: Bill Gurley, Dr. Carlos Steren, Tim Free, Gary Wynn, Sharon Marshall, Darrell Lay, Gail Cox, Traymon Allen, Professors Charles Feigerle, Craig Barnes, Fred Schell, and the department's administrative assistants, led by my personal advocate Rhonda Wallace.

To my wife, Mary-Helen Estes, I owe the greatest debt of gratitude. It was her love that has sustained me through my many years of study. She stood by me during good times and bad, always willing to give encouragement and support. Her compassion and patience have made her a greater wife than I ever could deserve and make her an excellent mother to our recently born son. Thank you so much, Mary, for taking such good care of both Evan and I, and for sharing your life with me.

ABSTRACT

As the Earth's population increases and natural resources decrease in supply, the development of new methods for energy storage and the efficient production of industrial chemicals becomes ever more important to humanity. The development of new nanomaterials may offer technological advances in the fields of sustainable energy production and storage, chemical production, medicine, and many others. The emerging field of nanoscience blends chemistry, physics, and engineering to create new materials that take advantage of properties found only on the nanoscale.

In this work, mesoporous silica spheres are used as a support for nanoparticles of palladium. This nanomaterial is shown to be an effective heterogeneous catalyst for the production of hydrogen peroxide from hydrogen and oxygen gases. This direct formation offers a more efficient route to the production of this important industrial feedstock without the use of anthraquinones, a class of organic chemicals used in current industrial production.

Graphene has received much attention in the last decade as a nanomaterial with many potential applications. Intense study of this one-atom-thick carbonaceous material has resulted in the publication of more than 7,000 journal articles in the year 2011 alone. Our work has focused on the chemical modification of graphene oxide to produce lithium-functionalized nanomaterials. As a two-dimensional scaffold, this material may have applications in hydrogen fuel cells and other advanced materials.

TABLE OF CONTENTS

Chapter Page

LIST OF TABLES

Table Page

LIST OF FIGURES

Figure Page

CHAPTER I

INTRODUCTION AND BACKGROUND

Nanomaterials: A Definition

The term "nanomaterial" is used to describe a broad subset of scientifically important materials. The material's size is of the most importance in determining whether or not the prefix "nano-" should be attached, but this is not the only consideration. Nanomaterials may be considered those that are of the scale 1 to 100 nanometers, or $1x10^{-9}$ to $1x10^{-7}$ meters, but this does not paint a complete picture of what encompasses a nanomaterial.

There are certainly many molecules that exceed 1 nanometer in diameter that would not be considered a nanomaterial. Porphyrins, for example, are relatively large molecules (some more than 1 nm in diameter and comprised of more than 100 atoms), but these are seldom referred to as nanomaterials. The difference largely lies in the fact that molecules act individually. In the case of many porphyrins, the center of the molecule acts as an Lewis base, donating electron density to metal atoms. Outer regions of the molecule may act to further stabilize this interaction or aid in the molecule's solubility. The point is that the molecule acts largely on its own, and doesn't necessarily act in concert with any neighboring porphyrins. This is an individual molecule, not a nanomaterial, regardless of its size.

On the other end of the "nano" length scale, many particles of 100 nanometers or less may still behave largely in the same way as bulk materials. Lead sulfide, for instance, in the solid state may be created in particles ranging from much greater than 1 micron to less than 5 nm in diameter. While these particles between 5 and 100 nm may all fit into the size range to be called "nano", those particles toward the smaller end of the scale behave differently than those nearer 100 nm. The difference lies in the particle surface area.

Surface phenomena are the major factors in nanochemistry. Atoms at the surface of a particle are more reactive than those on the inside. These surface atoms are often chemically unsaturated - that is, they have open coordination sites and could gain stability by reacting with additional atoms. The smaller PbS particles have much greater surface areas per volume than the larger particles. Above 100 nm in diameter, particles of crystalline PbS contains less than 5% of all atoms on their surface, but for particles below 8 nm, more than half of the atoms lie on the surface[1]. These surface-dominated particles are far more reactive than the relatively inert bulk material and have seen recent uses in photocatalysis[2] and in emerging solar cell technology[3]. PbS particles above 100 nm behave similarly to the bulk material and show no chemical or physical properties that suggests they would require a different nomenclature from that of much larger particles.

Exceedingly thin films may be very large in two dimensions, but still gain acceptance into the realm of nanoscience. Nanowires and nanotubes, similarly,

may be relatively lengthy in one dimension, but less than one nanometer in diameter. These nanomaterials often have very different physical properties than their bulk counterparts[4]. As these examples show, a nanomaterial is one whose properties are governed by the effects of quantum confinement and large surface-to-volume ratios, not simply one that fits into an arbitrary size range.

Uses and Importance of Nanomaterials

Ubiquity and Diversity of Current and Future Applications

Nanomaterials are increasingly used in medical and technical applications. From the drugs that enter our bodies to the exhaust that leaves our cars' tailpipes, nanomaterials color our everyday lives in many ways. Gold nanoparticles have been used since ancient times in China and Egypt to color ceramics[1]. Nanoparticles may be used to target specific parts of the body and release drugs more steadily over time than traditional methods, as is the case of cadmium sulfide-capped mesoporous silica spheres that have been used to deliver drugs into nervous system tissues[5]. Another medicinal use involves the selective heating of nanoparticles attached to tumor cells. Gold nanoparticles are heated using an infrared laser that does no damage to surrounding tissues. As the gold particles absorb the infrared photons, they release heat that destroys the cancer cells[6]. Nanotechnology has been applied to vehicle exhaust systems

design, resulting in lower carbon monoxide emissions and allowing for the use of less precious metal within the catalytic converters[7].

Perhaps the most important applications of nanomaterials are those yet to be fully developed. Titania nanoparticles in dye-sensitized solar cells offer the prospect of significantly greater energy production than traditional crystalline silicon solar panels[8]. A revolution in computer memory size may be realized by taking advantage of the spin-orbit coupling effect of semiconducting nanowires[9]. Further improvements in miniaturization and performance of computers and other electronics could also be realized through the use of graphene nanosheets and nanotubes, due to their high conductivity and speed of electron transport[10].

Nanoscale Heterogeneous Catalysis

Catalysts containing metal and metal oxide nanoparticles are ubiquitous in chemical manufacture but are also used increasingly in our daily lives. Nanoparticles of vanadium oxides deposited on titania, silica, and other support materials have wide industrial applications in the oxidative dehydrogenation of alkanes to form olefins[11]. Nanoparticles of chromium supported on porous silica, which is known as the Phillips catalyst, is used for the industrial preparation of polyethylene[12]. The production of olefins from synthesis gas, which may be obtained from biomass and other sustainable resources, may be accomplished using iron nanoparticles supported on alumina and carbon supports[13].

Apart from the chemical industry, nanoparticles of platinum, rhodium, cerium, barium, zirconium, lanthanum, and their oxides are used as catalysts to clean vehicle exhaust[7,14]. Nanoparticles of gold bound to titanium oxide are used in paints to catalytically clean carbon monoxide from the air[14].

Hydrogen Storage Materials

Electric motors operated by hydrogen fuel cells offer the potential to replace petroleum-based internal combustion engines in our automobiles, offering zero emissions at the tailpipe and the potential to reduce our dependence on fossil fuels. Among the greatest challenges in making hydrogen a competitive energy storage material is finding a suitable way to store hydrogen on board the vehicle. A great deal of research is currently underway to find nanomaterials that offer the ability to store large amounts of hydrogen within a small volume and will allow for efficient, repeatable adsorption and desorption of hydrogen.

The US Department of Energy (DOE) has set forth requirements for potential hydrogen storage materials related to their hydrogen uptake as a percentage of weight and volume[15]. These targets are used as goals for research projects and have been revised as more studies have been completed. The target weight percentage of hydrogen was 4.5% in 2010, with 5.5% being targeted for 2017, with an "ultimate" goal set at 7.5%. Volumetric capacity targets

for the same time periods have been set at 0.028, 0.040, and 0.070 kilograms of hydrogen per liter. It is useful to note that these are system requirements, including the weight and volume of storage containers, valves, and related equipment. Any system that meets the targets must therefore contain a storage material that far exceeds them.

Instrumentation

A diverse array of analytical techniques are used in the study of nanochemistry, from electron microscopy to adsorption isotherms. Many of the instruments required for these analyses are available either within the University of Tennessee Department of Chemistry, Department of Material Science, or at the nearby Oak Ridge National Laboratory. These tools are essential to the development of a true understanding of nanomaterials, as any one of these techniques can only provide an incomplete picture. It is important to understand nanomaterials on many length scales. Scanning electron microscopy (SEM) may provide information about particle size and shape, but infrared spectroscopy (IR) and x-ray photoelectron spectroscopy (XPS) provide details about the bonding energies between individual atoms of the particle. It is only through careful analysis of these complementary techniques that a complete understanding may be gained.

X-ray Powder Diffraction (XRD)

Powder diffraction of x-rays is a critical method of analysis in inorganic chemistry. Characterization of crystalline sample materials yields lattice parameters for the material, allowing for the identification of crystal phases, measurement of alloy composition, preferred orientation, particle size, and other structural information. Its use herein will be more limited in application: spacing between graphitic planes will be derived from the angle of x-ray diffraction. The relationships between this lattice spacing, *d*, the wavelength of x-ray radiation, *λ*, and the angle of diffraction, *θ*, is described by Bragg's law:

$$\lambda = 2\mathrm{d}\ \sin\theta$$

It is also pertinent to discussions herein that particle size is inversely proportional to diffraction pattern linewidth. This relationship is described by Scherrer's equation:

$$B = \frac{0.9\ \lambda}{t\ \cos\theta}$$

where *B* is the full width at half maximum of the diffraction peak in degrees 2*θ* and *t* is the diameter of the crystallites. 0.9 is a form factor used for particles of undetermined shape, but other numbers between 0.62 and 2.08 are used for particles of known shape [16-19].

Powder diffraction patterns presented herein were collected on one of two instruments. The primary instrument is a Philips PW1729 x-ray generator with Cu K_α source operating at 20 kV and 15 mA equipped with a capillary sample holder

stage and operated in the transmission mode. Powder samples are mounted in a 0.5 mm ID glass capillary, rotated at 1.0 rpm. The diffracted beam is detected by an INEL CPS120 constant position gas-filled transducer, operated under 15% ethane in argon, with 9.5 kV applied potential. This stationary 120° detector is positioned to detect scattered intensity in the range of 5º to 125º 2θ.

The second instrument used for the collection of x-ray diffraction data is a PANalytical Empyrean powder diffractometer. This instrument contains a Cu K_α x-ray source operating at 45 kV and 40 mA. The instrument employs Bragg-Brentano geometry operating in reflection mode, with a germanium incident beam monochromator and a PIXcel^{3D} charge-coupled device (CCD) detector.

Small Angle X-ray Scattering (SAXS)

Due to the inversely proportional relationship between scattering angle θ and d-spacing, low scattering angles can yield information about relatively large structural features compared to traditional x-ray powder diffraction. Scattering at small angles is frequently used to measure nanoparticle size[20] and repeating nanoscale features including mesoporous networks[21-23].

SAXS data was collected on a custom-built instrument produced by Molecular Metrology that includes a Cu K_α radiation source operated at 45 kV and 0.66 mA, a two-dimensional Gabriel wire detector, and two available sample-to-detector path lengths of 0.5 and 1.5 m. The instrument is operated under dynamic vacuum to reduce air scatter. Powder samples are mounted between

pieces of clear adhesive tape, which is a poor x-ray scatterer and can easily be subtracted from background intensities.

Solid-State Nuclear Magnetic Resonance

Nuclear magnetic resonance (NMR) spectroscopy is an analytical tool based on the interaction of nuclear spins with a magnetic field. Within a strong magnetic field, nuclear spin states are separated into energy levels. Nuclear spins may be excited into higher energy levels by absorption of photons in the radio frequency range, resulting in characteristic absorption spectra.

Since its development in the late 1940's, NMR has developed into the central source of chemical identification in most branches of chemistry. In the fields of organic chemistry, inorganic chemistry, and biochemistry, no other analytical tool is of greater importance. In the analysis of nanomaterials, it often serves a slightly less central role. For most chemical applications, the sample preparation involves preparing a dilute solution of the analyte within a glass tube. Many nanomaterial samples have poor solubility in standard NMR solvents as well as highly reactive surfaces, resulting in the necessity to use solid-state NMR techniques.

Solid-state NMR (and NMR in general) relies upon the Zeeman effect, which is the splitting of energy levels (in this case nuclear) in the presence of a magnetic field. The population of nuclei in the higher and lower energy states are nearly equal at room temperature, based on the equation:

$$N_{upper}/N_{lower} = 1 - 2\mu B_0/kT$$

where N_{upper} and N_{lower} are the number of spins in the upper and lower energy levels, μ is the magnetic moment of the nucleus, B_0 is the applied magnetic field, k is the Boltzmann constant, and T is the temperature of the nuclear spin system. For ^1H nuclei in a 9.39 Tesla magnetic field at room temperature, the value of N_{upper} / N_{lower} is roughly 0.99994, meaning that for every 1,000,000 nuclei in the sample, the difference in unperturbed populations is six nuclei. Since the magnetic moment in the direction of the applied field of the excited state cancels that of the ground state, only six in 1,000,000 hydrogen nuclei are capable of creating a measurable signal by absorbing radio frequency energy[24]. While this signal can be increased by increasing the applied magnetic field or decreasing the temperature, modern spectroscopy uses resonance techniques to polarize all of the spins in the lower energy state, resulting in a much larger net magnetization in a direction perpendicular to the applied magnetic field[24].

The analysis of solid-state samples presents unique challenges to produce narrow, highly resolved, individual peaks characteristic of spectra obtained from samples in solution. The main contributors to the broadening of spectral lines obtained from solid samples are chemical shift anisotropy, static dipolar interactions, and, in the case of many samples, quadrupolar interactions[25]. In solution and gas phase studies, molecules within a sample are assumed to rapidly rotate independent of one another. The result of these rapid reorientational motions is to average out any differences in shielding about the

nucleus of interest. Hence the measured spectrum will appear as a well-resolved average of the many possible orientations of the nuclei present in the sample. In most solid samples (especially at low temperatures), molecules do not freely rotate, resulting in a variety of possible molecular orientations being represented in an obtained spectrum. This results in a broad, poorly resolved set of peaks of low intensity. Similarly, dipolar interactions between nuclei in the sample are affected by the orientation of each nuclear spin with regard to each other. Because solid samples may have nuclei with many orientations, the possible dipolar interactions may span many kilohertz in energy, which also will result in the broadening of the observed spectral peaks. Quadrupolar interactions include those effects caused by nuclei with non-spherical electric charge distributions, which, in a solid sample, may have many possible orientations. Magic angle spinning (MAS) is a technique frequently used in solid-state NMR to effectively remove these contributions to line broadening. The functional form that describes these effects contains an anisotropic (angular-dependent) term that includes the factor ($3\cos^2\theta - 1$). The “magic” angle is the angle θ which causes this term to be zero[26]. Hence when the NMR sample is spun at the "magic" angle of 57.47º with respect to the static magnetic field, the chemical shift anisotropy, static dipolar interactions, and first-order quadrupolar contributions to the line broadening effectively disappear, if the sample is spun at a significantly high rate. With these three contributions removed, a major improvement in spectral resolution is realized[27].

All solid-state NMR spectra presented herein were collected on a Varian INOVA 400 MHz instrument with a wide-bore, 9.392 T magnet. The system is equipped with a Chemagnetic 5 mm MAS probe capable of 12 kHz sample rotation with proton and broadband multinuclear channels.

Vibrational Spectroscopy

Infrared and Raman spectroscopy are useful, complementary tools in the analysis of nanomaterials. Both techniques use a light source to probe the vibrational energies of a studied material, providing information on the presence of functional groups as well as other information about the material.

Active vibrational modes for infrared spectroscopy are those which result in a change in the studied molecule's electric dipole moment. For a vibrational mode to be Raman active, that vibration must result in a change in the molecule's polarizability within an electric field. Molecular symmetry governs which modes affect a molecule's dipole moment and polarizability, but when the samples being studies are nanoparticles with many hundreds of atoms rather than single molecules, symmetry is generally very low, yielding all vibrational modes both infrared and Raman active.

Infrared spectrometers use a light source with wavelengths between 2.5 and 15 micrometers. Photons in this frequency range are in an energy range needed to activate vibrational modes present in the sample. The instrument compares the intensity of light from the source to the intensity of light passed

through the sample and plots the difference between the two (absorbance) as a function of energy, which is traditionally reported in wavenumbers (cm^{-1}).

Raman spectroscopy utilizes a higher energy light source of a single frequency, usually in the visible range. When the sample is illuminated, the vast majority of light passes through the sample unaffected. Less than 1%, however, is scattered in all directions. Light that scatters at the original frequency is known as Rayleigh scattering. This makes up the majority of the scattered light. A small amount, however, has a frequency that varies from the incident light by an amount equal to the vibrational energies of the sample. This scattering is known as Raman scattering, and may be either higher or lower in energy than the incident light. Of this Raman scattered light, light that is scattered at a reduced energy is called Stokes radiation and light scattered at increased energy is called anti-Stokes radiation[28].

Raman spectroscopy was performed using a JY-Horiba T64000 spectrometer equipped with a 514.5 nm edge filter, 600 gr. mm^{-1} grating, 514.5 nm laser excitation and CCD detector. The incident laser beam was focused onto the sample materials through a 50X objective forming a laser spot size of 2 μm. The instrument resolution is approximately 2 cm^{-1}.

Inductively Coupled Plasma - Optical Emission Spectroscopy (ICP-OES)

ICP-OES is a method for elemental quantitative analysis. Dilute aqueous samples may be measured against calibration standards for most elements of

the periodic table, though the technique is most often used for metal concentration determination. An argon plasma is used to ionize atoms from within a sample solution, yielding element-specific emission spectra. These characteristic spectra are measured by a visible wavelength spectrometer. Comparisons of sample emission spectra versus spectra recorded for calibration standards yield highly accurate concentrations[27]. ICP-OES was performed on a Perkin Elmer Optima 2100 DV instrument.

X-ray Photoelectron Spectroscopy (XPS)

XPS provides information about atoms located in the surface region of sample by collecting with electrons emitted from depths of approximately 1 to 3 nm for most materials[29]. Not only is elemental data provided, but also information about the chemical environment experienced by atoms present at the material surface.

To obtain this information, samples are bombarded with x-rays held within an ultrahigh vacuum chamber. The interaction of the x-ray photons with atoms within the sample causes electrons to be ejected. The kinetic energy of these ejected electrons is measured, yielding information about the atom from which the electron originated. The binding energy (E_B) of the ejected electron can then be calculated using the following equation:

$$E_B = h\nu - KE_e - W$$

where $h\nu$ is the energy of the incident x-ray, KE_e is the kinetic energy of the ejected electron and W is the work function of the XPS instrument, all three of which are known[29].

XPS measurements were taken on a Thermo Scientific K-alpha instrument with Al K_α radiation source located at the High Temperature Materials Laboratory at Oak Ridge National Laboratory (ORNL).

Scanning Electron Microscopy (SEM) and Transmission Electron Microscopy (TEM)

SEM and TEM are useful tools for the study of materials, yielding images of materials with great detail as to their complex surfaces that may be impossible to obtain otherwise. SEM is the technique of lower resolution, offering information on the order of tens of nanometers and above, while the most advanced TEM instruments are capable of atomic resolution.

In both SEM and TEM, an electron gun is focused on a sample through the use of magnetic lenses. Electrons, accelerated through a large potential, bombard the sample under vacuum. In TEM, electrons transmitted through the material are measured, while in SEM, backscattered electrons and less energetic secondary electrons ejected from the material's surface are measured[27]. Unlike the transmitted electrons in TEM, these backscattered and secondary electrons contain no direct information about the sample material. An SEM image is instead produced by measuring reflected intensities in all directions at each

location on the sample, which are then added together to form an intensity map of the material surface[27].

SEM was performed using a Hitachi S4700 at the Center for Nanophase Material Science at ORNL. TEM was performed within the Material Science and Technology Division of ORNL using a VG Microscopes HB603A operating at 300 kV. The microscope has a Nion spherical aberration-corrector and can obtain a resolution below 0.8 Å[30].

Adsorption Isotherm

Adsorption isotherm measurements allow for a detailed view of the interactions between a solid substrate and an adsorbed gas. Small molecules are adsorbed from the gas phase onto the surface of a sample material at low temperature. The subtle changes in overpressures of the adsorbed gas are recorded and plotted versus the number of moles of gas introduced to the sample. These plots quantify the amount of gas adsorbed by the sample, and when coupled with information about the size of the gas molecule used, the surface area of the studied material can be determined.

Adsorption isotherm measurements reported herein were performed using a high-resolution volumetric adsorption isotherm systems designed and built by the group. These systems contain a gas handling manifold equipped with air-actuated valves, a sample cell with mounted temperature probe, a helium compressor, displex, temperature controller, pressure transducer, turbomolecular

vacuum pump, and proprietary software created using the LabView programming language[31].

CHAPTER II

THE DIRECT FORMATION OF HYDROGEN PEROXIDE

Motivation

Current Methods of Production

Hydrogen peroxide is an important industrial feedstock, with nearly 700,000 tons of H_2O_2 consumed in the year 2000 in North America alone[32]. The major use of H_2O_2 is as a bleaching agent in the production of paper. It is also used to bleach textiles, as an oxidant in the industrial production of chemicals, and as a reducing agent in the treatment of waste water containing hypochlorite and other strong oxidizers[32].

The vast majority of H_2O_2 is produced by variations of the Riedl-Pfleiderer process, developed in Germany during World War II. This process relies on the oxidation and reduction of anthraquinones, a class of aromatic organic compounds shown in scheme 1. At elevated temperature and pressure, O_2 and anthrahydroquinone react to form H_2O_2 and anthraquinone. Anthrahydroquinone is then regenerated by the reduction of anthraquinone with H_2 and a heterogeneous Pd catalyst. Unwanted side reactions include the reduction of the unsaturated aromatic portions of anthrahydroquinone molecules which decreases the rate of H_2O_2 production. Regeneration of anthraquinone starting materials is therefore important to the manufacturing process and has been

studied extensively by the chemical industry, including Mitsubishi[33], FMC[34], and Du Pont[35]. The regeneration process is resource intensive, utilizing organic solvents and reagents as well as oxidation catalysts to reform the expensive anthraquinone species.

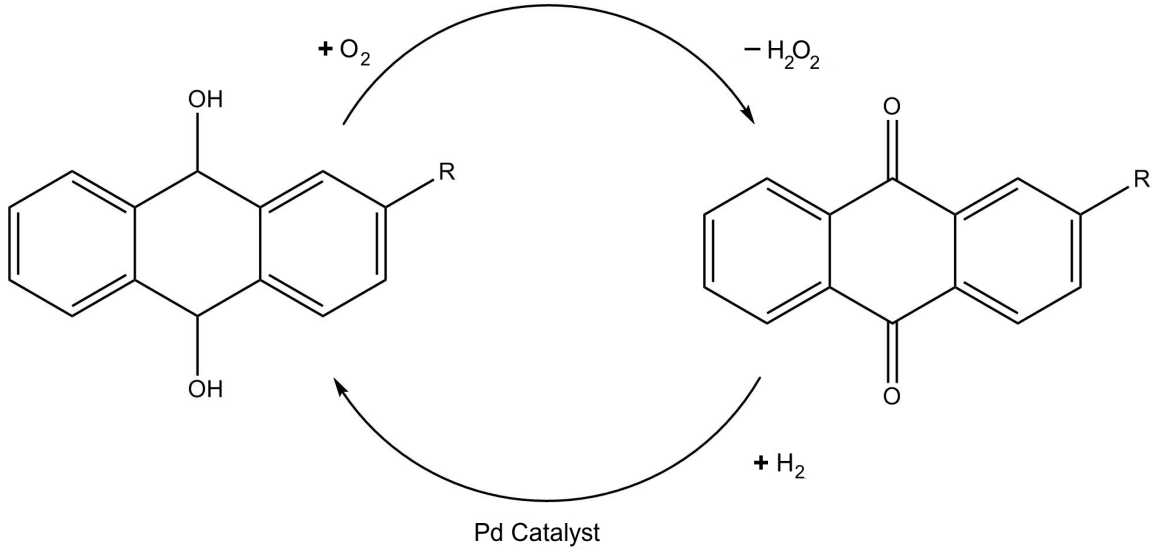

Scheme 1

Heterogeneous Catalysts for Direct Formation

The direct formation of hydrogen peroxide from H_2 and O_2 gases has been known for at least 50 years[36]. In the past ten years, advances in the production of catalysts have made this method of production ever more viable as an industrial option[37-46]. Scheme 2 shows the simple reaction scheme. The pathway to this formation involves the dissociation of H_2 to form a metal hydride intermediate at the catalyst surface, which then reduces molecular oxygen to form hydrogen

peroxide. Catalysts chosen for this reaction therefore require an affinity for molecular hydrogen and are generally made from palladium, gold, or a combination of the two.

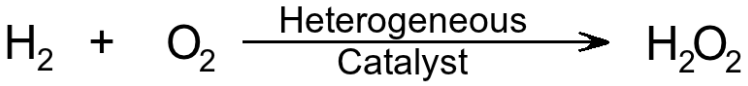

Scheme 2

The reaction is generally carried out in aqueous or organic solution, with the gaseous starting materials bubbled through the liquid phase. The metal catalyst is most often supported on a metal oxide or carbonaceous support. Studies have found that bromide salts may act as a promoter, which can increase the rate of conversion and selectivity toward production of H_2O_2 by poisoning the catalytic production of H_2O[37]. It has also been shown that choice of solvent also affects both conversion and selectivity with a mixture of ethanol and water yielding the greatest results[37]. The presence of acid in the reaction solution has been shown to decrease the base-catalyzed decomposition of H_2O_2, with phosphoric acid being an advantageous choice because phosphate ion is frequently used as a stabilizing agent in H_2O_2 solutions[37].

The role of the transition metal catalyst in the direct formation of the gases tinto H_2O_2 has been shown to proceed without the dissociation of molecular oxygen into individual atoms[46] and is thought to contain an HO_2 intermediate[36].

These observations are consistent with a reaction mechanism that involves a three-step process as depicted in scheme 3. The first step is the oxidative addition of H_2 onto the palladium catalyst, which results in cleavage of the molecular hydrogen bond to form a dihydride upon the catalyst surface. Step two requires the 1,2−insertion of molecular oxygen into one of the Pd−H bonds, resulting in the formation of a Pd−O−O−H intermediate. The final step would be the release of H−O−O−H by the reductive elimination of −O−O−H and the remaining hydride from the palladium surface.

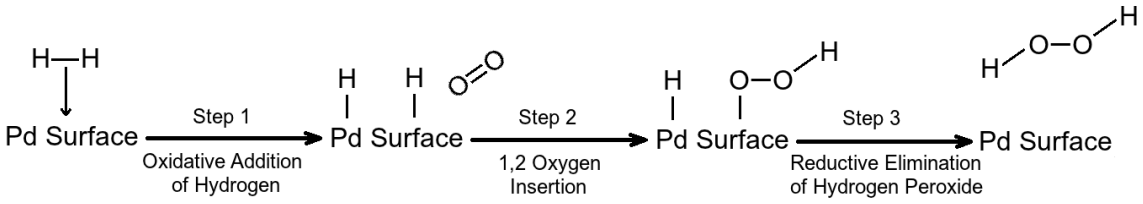

Scheme 3

Catalysts in the literature most often involve supports made from carbon[37,43-45] or oxides of aluminum[37,43], cerium[37], iron[37], magnesium[43], or titanium[37,43]. Very little attention seems to have been paid to silica-based supports, specifically those with exceptional surface area[38-42]. The work described herein has focused on this area, with a high surface area support of palladium nanoparticles being investigated as a potential catalyst for the direct formation of H_2O_2.

Synthesis

Mesoporous Silica Substrate

In our laboratory[46], mesoporous silica spheres have been prepared following a well-known protocol[1,47]. This method uses the combination of a micellular formation technique and standard sol-gel methodology to create organic micelles around which silica spheres are formed. Micelles are formed by the dissolution of a surfactant, in this case hexadecyltrimethyl ammonium bromide (CTAB), in water. This amphiphilic salt contains a 16-carbon hydrophobic "tail" attached to a hydrophilic ammonium bromide "head" as shown in figure 1. If the CTAB concentration is great enough, the non-polar tail sections align such that their exposure to water is minimized by forming tubes, with the positively charged ammonium head of each molecule facing outward towards the aqueous solution. Tetraethyl ortho-silicate (TEOS) and a base (often ammonium hydroxide) are added to the solution, gradually forming spheres of condensed silica as the ethyl ligands of TEOS are hydrolyzed by the basic solution. Micelles, already present in the solution, are incorporated into the silica spheres as they form and result in a hexagonal arrangement within the particle. These spheres are collected, washed, and calcined to remove the organic micelles, leaving behind hexagonally arranged pores within the silica spheres.

During a typical synthesis of silica spheres as depicted in scheme 4, a 2000 mL round-bottom flask is equipped with a Teflon-coated, magnetic, stir bar.

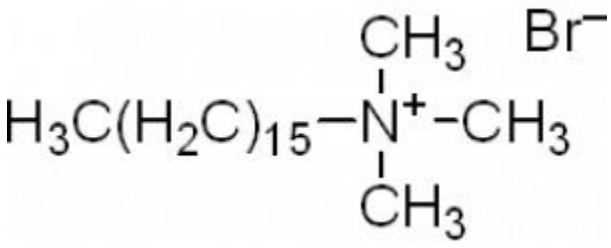

Figure 1: The amphiphilic CTAB molecule contains an ionic "head" and a non-polar "tail".

In this vessel, 58.5 mL of NH_4OH (14.8M, Fisher, ACS Plus) is dissolved in 1100 mL of deionized water. After this basic mixture is vigorously stirred for five minutes, 3.02 g of CTAB (99+%, Sigma) is added slowly to ensure complete dissolution of the salt. After another hour of stirring, 14.7 mL of TEOS (99.0+%, Fluka) is added dropwise into the solution. This mixture is allowed to stir overnight as a milky white precipitate forms in the flask. On the following day, the mixture is filtered via a fine glass frit using a vacuum aspirator and side-armed Erlenmeyer flask. A white solid is collected atop the frit, which is washed with five 15 mL aliquots of deionized water and two 15 mL portions of 190 proof ethanol. The product is further dried overnight at ~35 °C, then calcined in air using the following temperature profile: room temperature to 120 °C over thirty minutes, held at 120 °C for five hours, then heated to 550 °C over seven hours, where it is held for eight hours more before returning to room temperature.

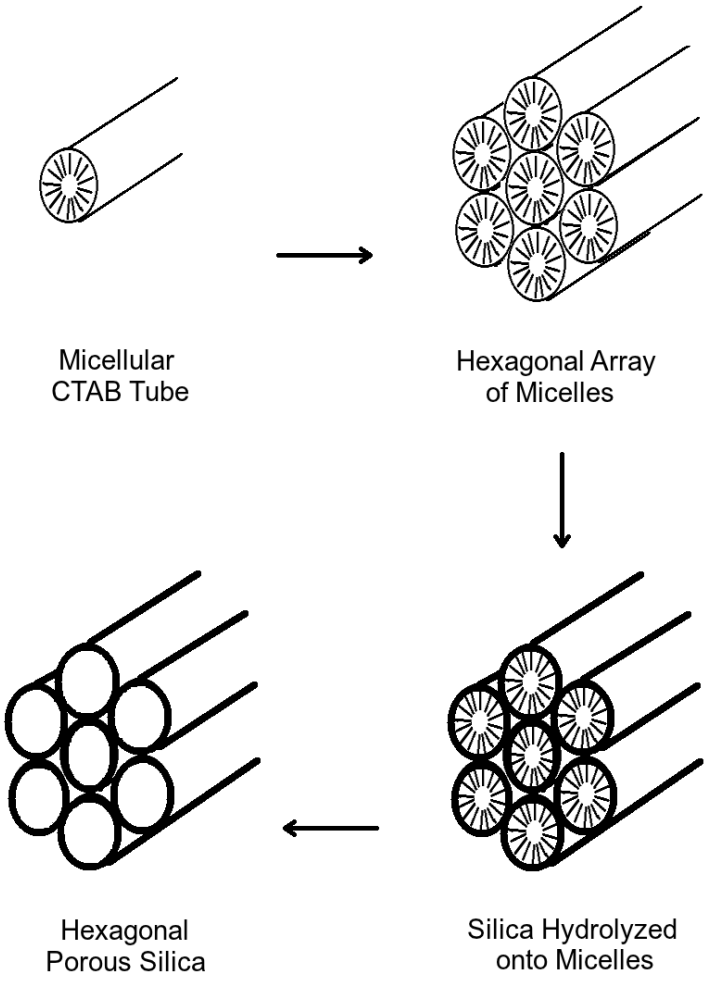

Scheme 4

Palladium Nanoparticle Impregnation

Palladium nanoparticles are formed within the mesopores of the silica spheres by dissolving a palladium salt into a solvent in the presence of the spheres, followed by evaporation of the solvent to immobilize the metal salt. The salt is then converted to zero-valent palladium metal by reduction of the salt

through either thermal or chemical methods. Heat treatment results in sintering of the metal to form nanoparticles within the pores, which act as a template that controls the ultimate size of the metal nanoparticles.

In a typical preparation, as depicted in scheme 5, 5 mg of palladium(II) acetate (trimer, 98+%, Strem) is added to 170 mg of calcined mesoporous silica spheres, prepared as described above. The metal salt is dissolved in roughly 10 mL of acetone (99+%, Fisher) in a 50 mL round-bottom flask with 24/40 ground glass neck. The flask is placed in an ultrasonic bath for 30 minutes, then attached to a rotary evaporator, where the solvent is removed at 40 °C under a mild vacuum over one hour. A homogenous, light yellow powder is obtained, which is placed in a 2 cm-long boat-shaped vessel within a flow-through quartz reaction tube. This tube, including the palladium-containing silica spheres, is placed in a furnace and purged of air with 4% hydrogen in argon (UHP, Airgas) for 10 minutes. The furnace is heated to 250 °C for 2-3 hours while a modest flow (roughly 10 sccm) of hydrogen/argon gas is passed through the tube, yielding a gray powder which has been determined to be fully reduced Pd^0 nanoparticles within the mesoporous silica spheres.

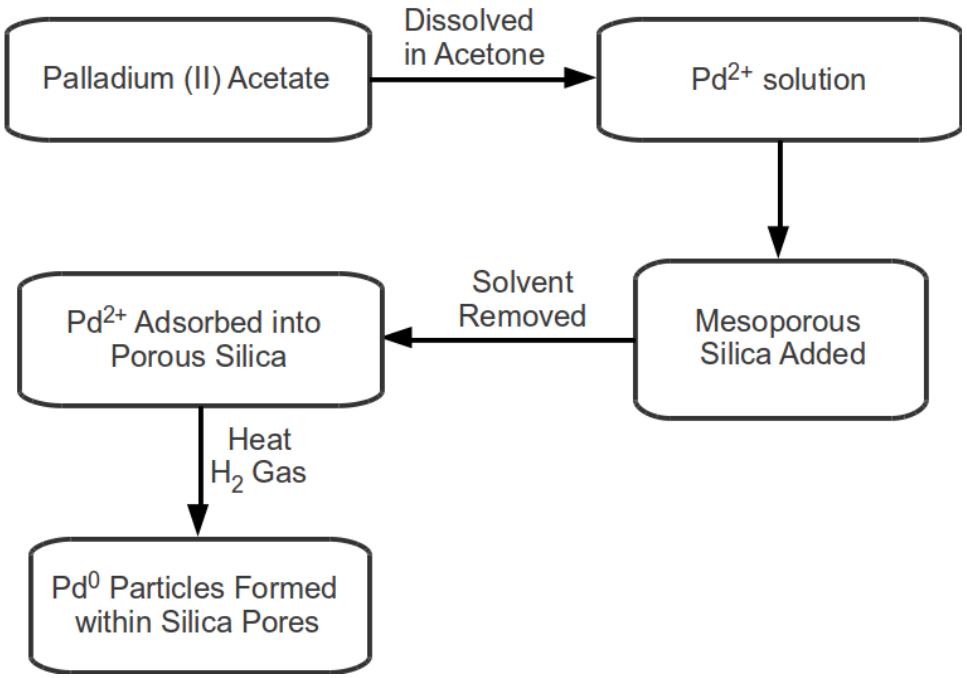

Scheme 5

Chitosan-Chelated Nanoparticles

Chitosan is a water-soluble, long-chained, linear polysaccharide comprised of random units of glucosamine and its N-acetyl derivative, with a high abundance of free amine groups (see Figure 2) derived from chitin, a protein found in the exoskeleton of crustaceans[48]. Due to its strong tendency to complex with metal ions, insolubility in the vast majority of solvents and its physical and chemical versatility, chitosan has been increasingly used in the synthesis of nanocatalysts[49-51].

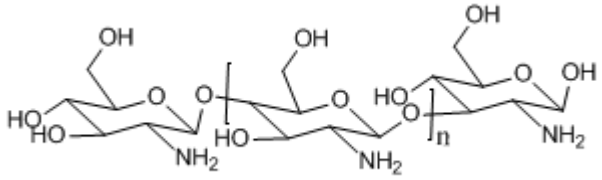

Figure 2: Chitosan is a polysaccharide with free amine groups which may be used to chelate to transition metals

To compare its effect on catalytic activity to our previously prepared catalyst, chitosan was incorporated into the pores of mesoporous silica spheres prior to introduction of palladium, as shown in scheme 6. In a typical preparation, 90 mg of dry, calcined mesoporous silica spheres were placed in a 50 mL round-bottom flask along with 5.9 mg of chitosan (avg. mol. wt.: 1,000 - 3,000 g/mol, Kitto Life Co., Kyongki-Do, S. Korea). To this dry mixture, 25 mL of deionized water was added. The flask was placed in an ultrasonic bath for 90 minutes to allow for the dissolution of the water-soluble chitosan. A translucent yellow solution was observed, with white silica particles settled at the bottom of the flask. The flask was fitted to a rotary evaporator where solvent was slowly evaporated under a mild vacuum at 40 °C, leaving only a homogenous pale yellow powder, which is further dried at 70° overnight to remove any residual water.

Palladium is incorporated without disturbing the previously added chitosan by taking advantage of the insolubility of chitosan in organic solvents, including acetone. To 95 mg of the chitosan-incorporated silica powder, 3.0 mg of palladium(II) acetate was added in a 50 mL round-bottom flask along with 25 mL

of acetone (ACS grade, Fisher). The mixture was again placed in an ultrasonic bath for 90 minutes and solvent was removed through the use of a rotary evaporator.

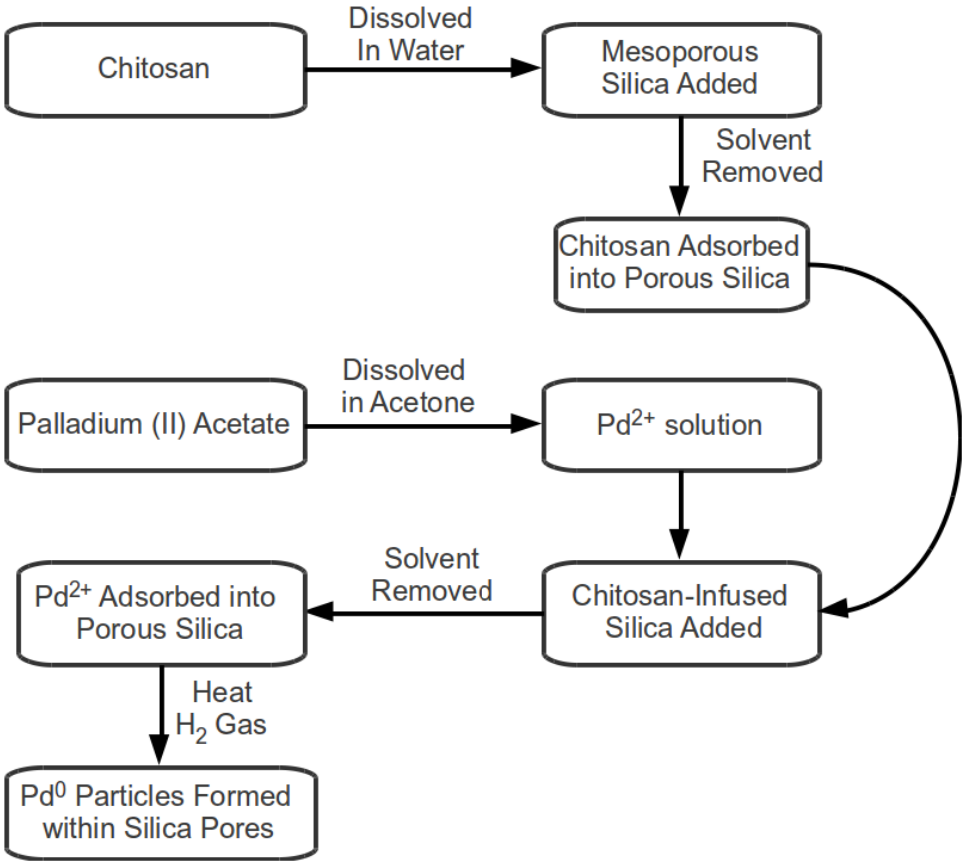

Scheme 6

Once thoroughly dried, the pale yellow powder was placed into a sample boat within a quartz flow tube. The incorporated palladium was then reduced under a flow of 4% H_2/Ar at 90 - 105 °C over 30 minutes, yielding a gray powder. Note that a milder reduction temperature was used in comparison to the non-chitosan incorporated samples in an attempt to minimize damage to the bio-polymer.

Materials Characterization

XRD

Due to the amorphous nature of the mesoporous silica spheres, no discernible diffraction patterns greater than background noise were obtained by standard powder diffraction techniques. Likewise, no palladium signal was obtained, possibly due in part to both the low weight percentages of palladium in the samples (between 1% and 2%) and their small particle size (less than 3 nm) which increases broadening of any diffraction peak that may have otherwise been present.

SAXS

For samples of both palladium-doped and undoped mesoporous silica spheres, SAXS clearly shows diffraction peaks associated with a hexagonal array of pores. Diffraction peaks from the (1,0), (1,1), and (2,0) 2-dimensional hexagonal lattice are labeled in each (Figure 3)[52,53]. As labeled in the figure, MSS refers to mesoporous silica spheres (the undoped support material) while MSS-Pd-R refers to the palladium-loaded, hydrogen-reduced, mesoporous silica spheres. While intensity measurements were not quantitative, the relative decrease in peak height of the pattern from the Pd-doped spheres compared to the bare material suggests increased disorder in the hexagonal lattice. This is likely due to some of the palladium particles residing outside of the pores on the

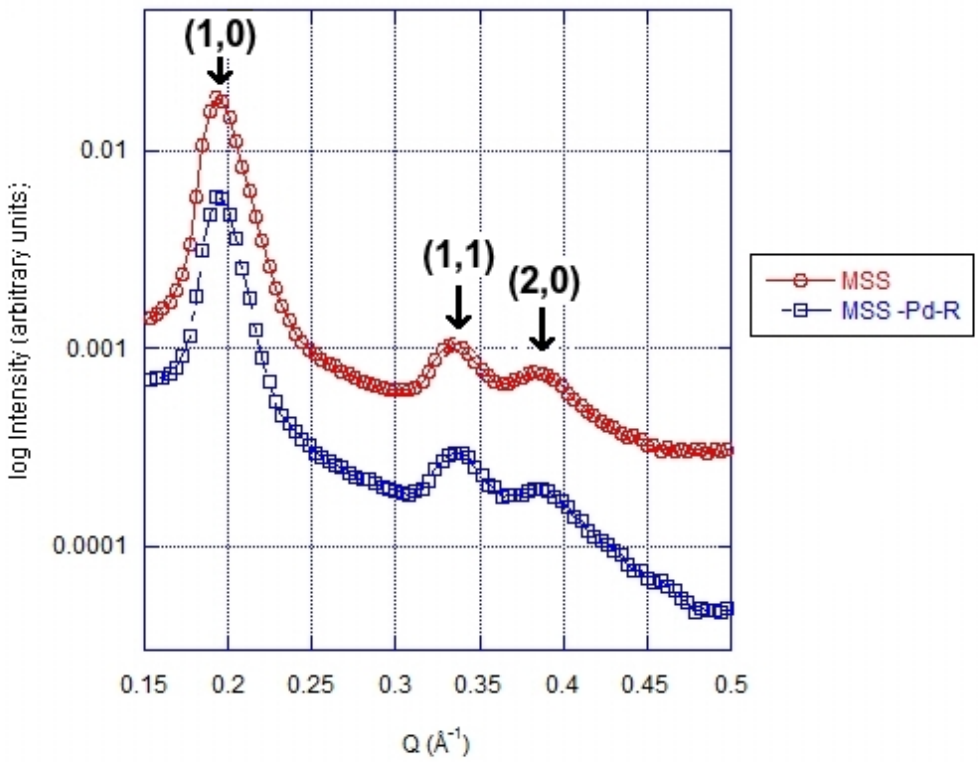

Figure 3: SAXS Comparison of Mesoporous Silica Spheres both with and without Pd Nanoparticles

surface of the sphere[53,54]. Correlation between the peak locations, d-spacing, and the lattice parameter, A, are summarized in a table that appears in the appendix (table 1).

ICP-OES

Samples were prepared by desorption/oxidation of the palladium nanoparticles from their silica substrate by placing the palladium-impregnated sphere samples in an aqueous solution of 30% freshly prepared *aqua regia* and an ultrasonic bath for 30 minutes. Five calibration standards of greater and lesser palladium concentration were prepared using palladium(II) chloride salt (99+%, Strem) dissolved in a mixture of deionized water and 30% *aqua regia*.

Samples of Pd-doped spheres, though prepared similarly, were found to have slightly different weight percentages of Pd, presumably due to errors in delivery of the small amounts of palladium(II) acetate required during synthesis. ICP-OES was useful for the exact determination of palladium weight percentage in samples, which allowed for a direct comparison of catalytic performance. A table of palladium loadings and ICP-OES results appears in the appendix (table 2).

SEM and TEM

SEM images of both doped and undoped spheres appear identical at the SEM length scales, as was expected. Since the palladium particles were expected to have formed within the mesopores of the silica particles, their size

was predicted to be no larger than 3 nm. Particles of this size are far smaller than the resolution of the SEM instrument. Silica spheres of near uniform size are shown in figures 4 and 5 and are representative of all samples produced. Spheres range from 300 to 500 nm in diameter.

Z-contrast resolved TEM images of palladium-doped spheres (figure 6) clearly contain Pd nanoparticles (lighter colored spots) within the porous silica substrate as well as a small amount of Pd adsorbed onto the surface of the spheres. The ordered porous silica network is also visible. Note that the external Pd particles appear larger in diameter than those embedded within the pores. Particle growth within the pores is limited by pore diameter, while those on the surface may grow larger during the thermal reduction process.

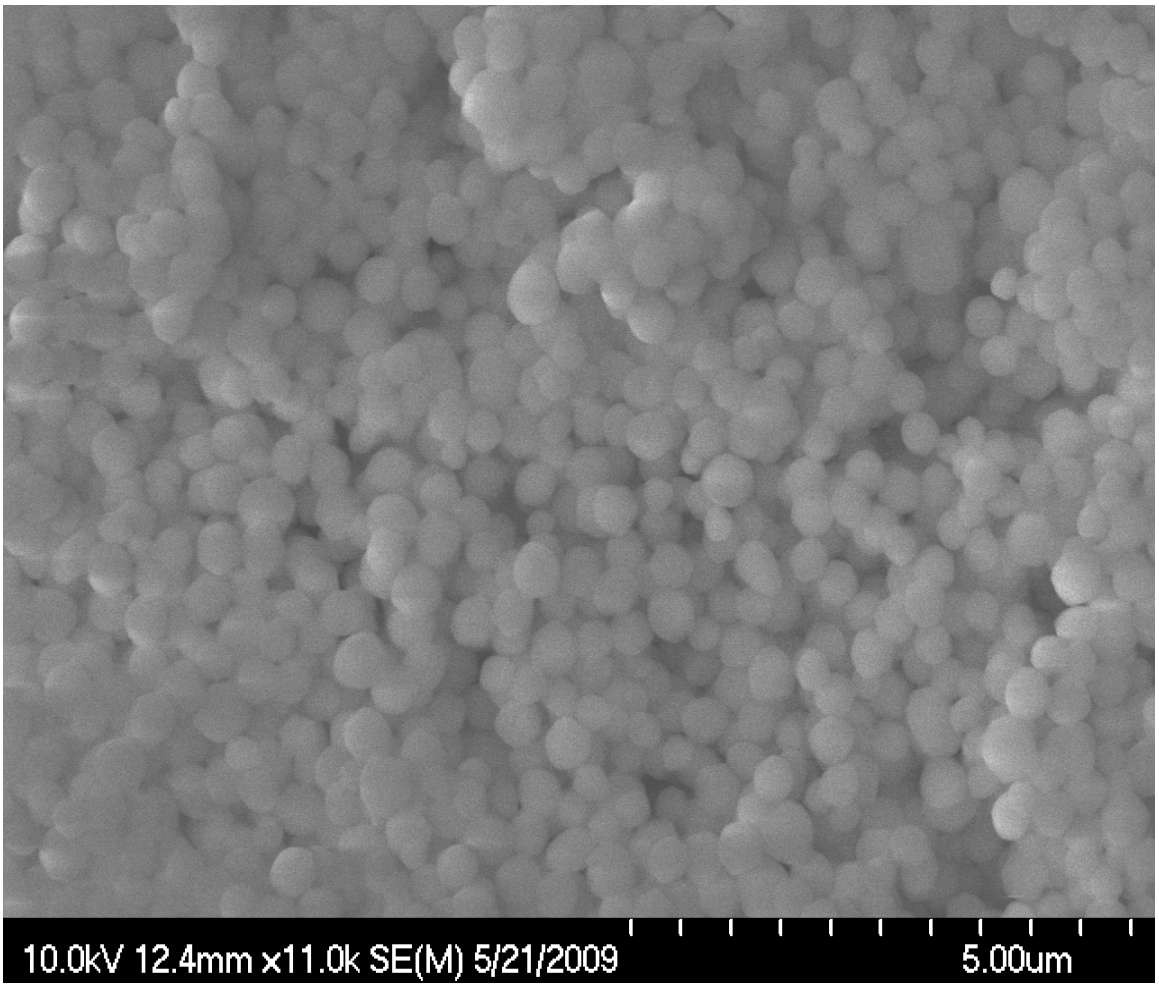

Figure 4: SEM Image of Mesoporous Silica Spheres without Embedded Pd Nanoparticles

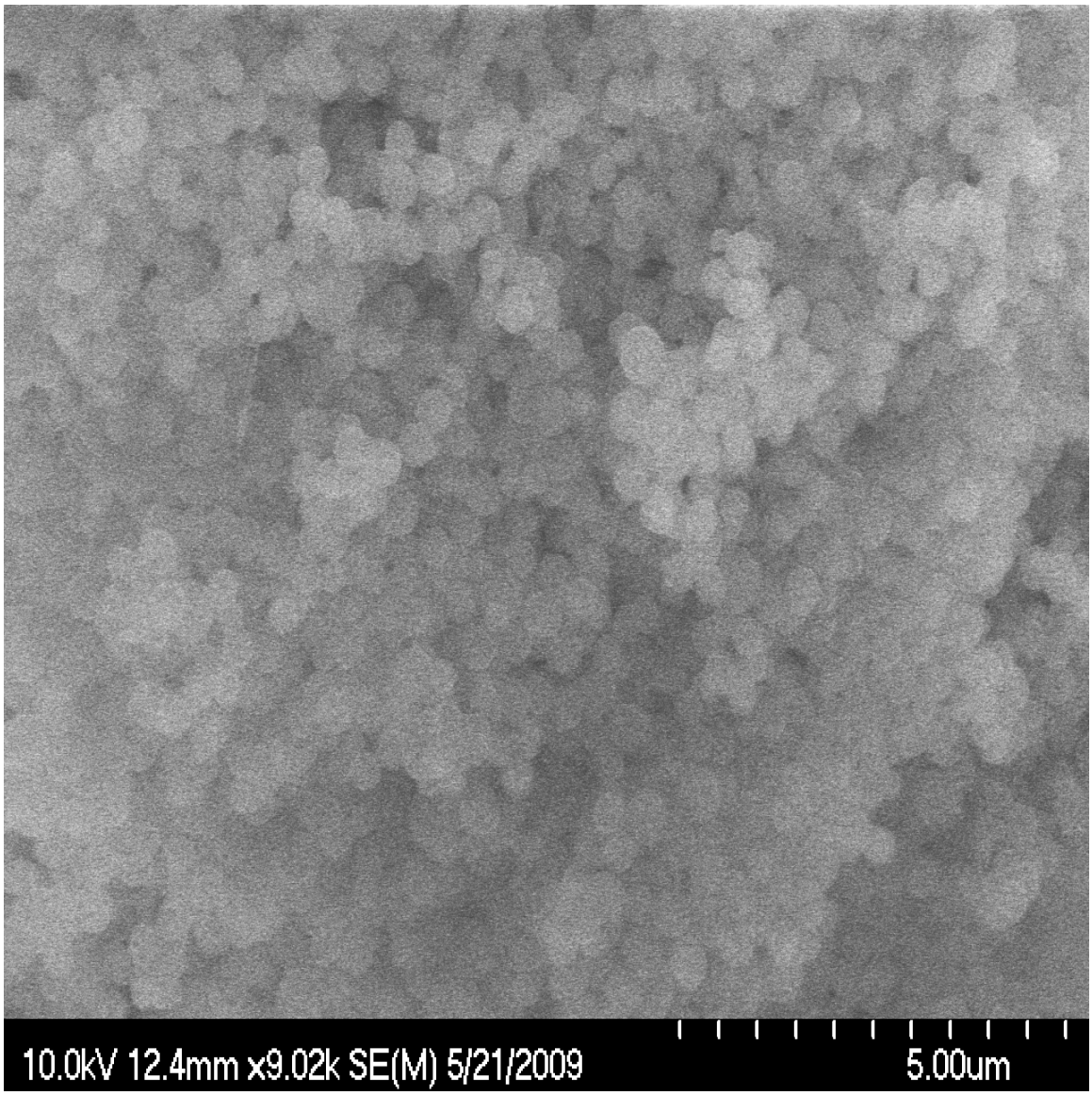

Figure 5: SEM Image of Mesoporous Silica Spheres Prepared with Embedded Pd Nanoparticles

Figure 6: Z-Contrast TEM Image Showing Pd Nanoparticles Embedded within a Mesoporous Silica Sphere

Catalytic Performance

Experimental Apparatus

Catalytic experiments were performed using a Teflon-lined, stainless steel reaction vessel built to withstand high pressures (figure 7). In a typical reaction, 30 mg of ~1.5 wt% palladium-impregnated mesoporous silica spheres were placed in a solution containing 25 mL of 1.6 M H_3PO_4 and $6x10^{-4}$ M sodium bromide, 25 mL of 190 proof ethanol, and a Teflon-coated magnetic stir bar. **It is important that <u>all of the</u> palladium-decorated material is within the solution** (i.e. – the walls of the reaction vessel are free of even minute amounts of palladium on silica) **to avoid a possibly explosive reaction!** In order to remove any residual air from the reaction vessel, it is purged three times with oxygen gas (99%, Airgas) initially pressurizing the vessel to 240 psi. The reaction vessel is finally charged with 240 psi O_2 and 75 psi H_2 (99%, Airgas) and stirring is commenced. 2 mL aliquots of the liquid phase are siphoned from the vessel every 60 minutes for 5 hours and titrated in sulfuric acid against a potassium permanganate solution, which undergoes the redox reaction with H_2O_2 shown in scheme 7.

$$2\ (5\ e^- + 8\ H^+ + MnO_4^- \rightarrow Mn^{2+} + 4\ H_2O)$$
$$\underline{5\ (\ H_2O_2 \rightarrow O_2 + 2\ H^+ + 2\ e^-)}$$
$$6\ H^+ + 2\ MnO_4^- + 5\ H_2O_2 \rightarrow 2\ Mn^{2+} + 8\ H_2O + 5\ O_2$$

Scheme 7

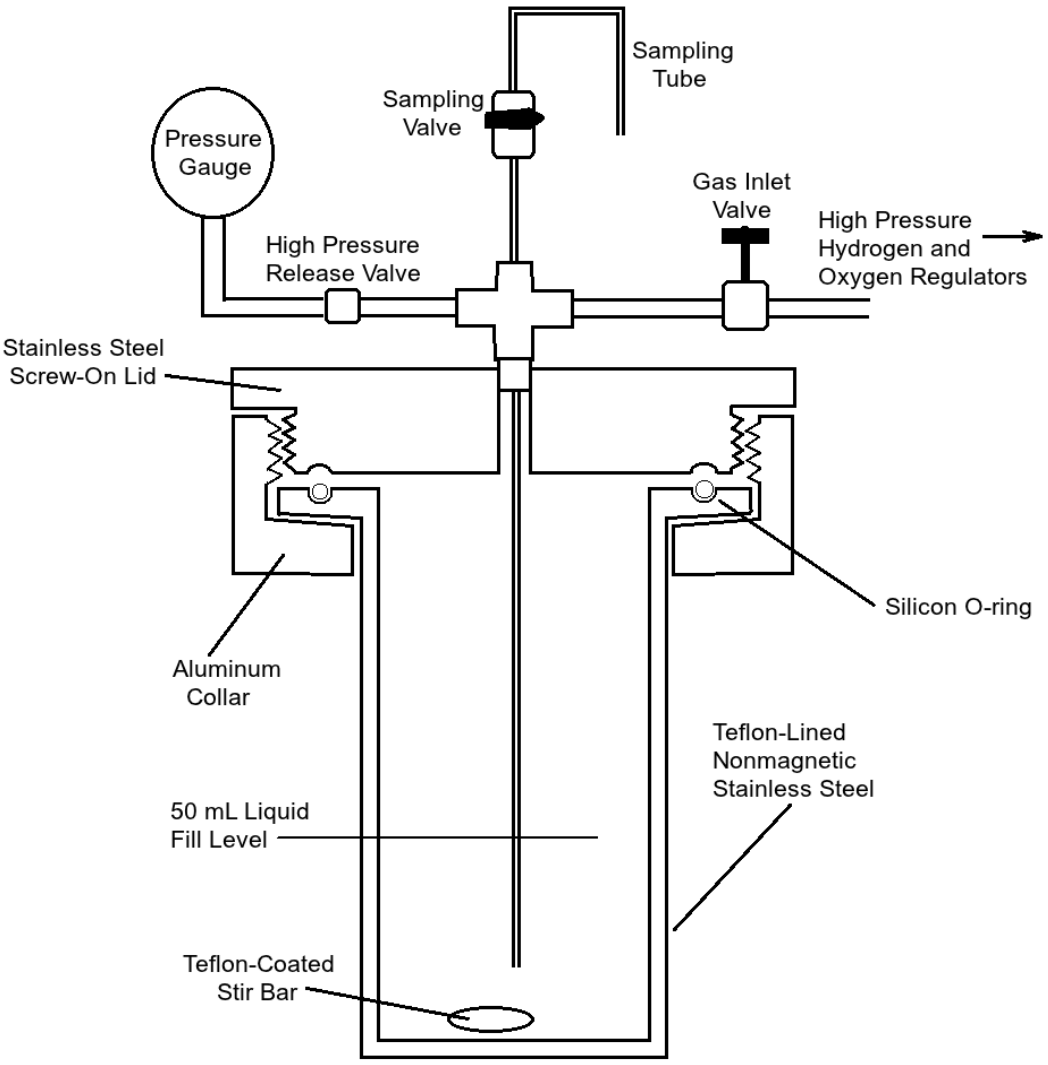

Figure 7: High Pressure Reaction Vessel for the Measurement of Heterogeneous Catalyst Performance

Production of Hydrogen Peroxide

Catalyst activity was measured hourly and compared to other palladium-containing materials as well as to literature values. Turnover Factor (TOF) is defined here as moles of H_2O_2 per moles of Pd per hour. Figure 8 shows a graph of the comparison between four Pd-containing materials. Samples of Pd-doped mesoporous silica spheres, labeled MSS-3Pd, and MSS-3Pd + Chitosan were prepared as described above. To compare the effects of pore size of silica, a sample of the palladium-doped SBA-15 was used as well. SBA-15 is similar to our porous spheres in that it also contains hexagonally-arranged pores into which metal particles may be adsorbed, but differs in that the pores are of larger diameter. Pore diameter of the comparison sample were 8 nm. A final comparison was made to a sample of palladium particles deposited onto the surface of tetrapod-shaped nanoparticles of zinc oxide.

Comparison of the samples shows that the palladium-doped mesoporous silica spheres outperform the other doped nanomaterials. While Pd-doped SBA-15 shows a greater initial rate of reaction, the rate of reaction falls precipitously. It is hypothesized that this is due to leaching of the particles out of the larger pores, resulting in the destruction of the catalyst. The smaller-pored silica spheres afford greater physisorption between the metal particles and the silica scaffold, resulting in a much less pronounced loss of activity over time.

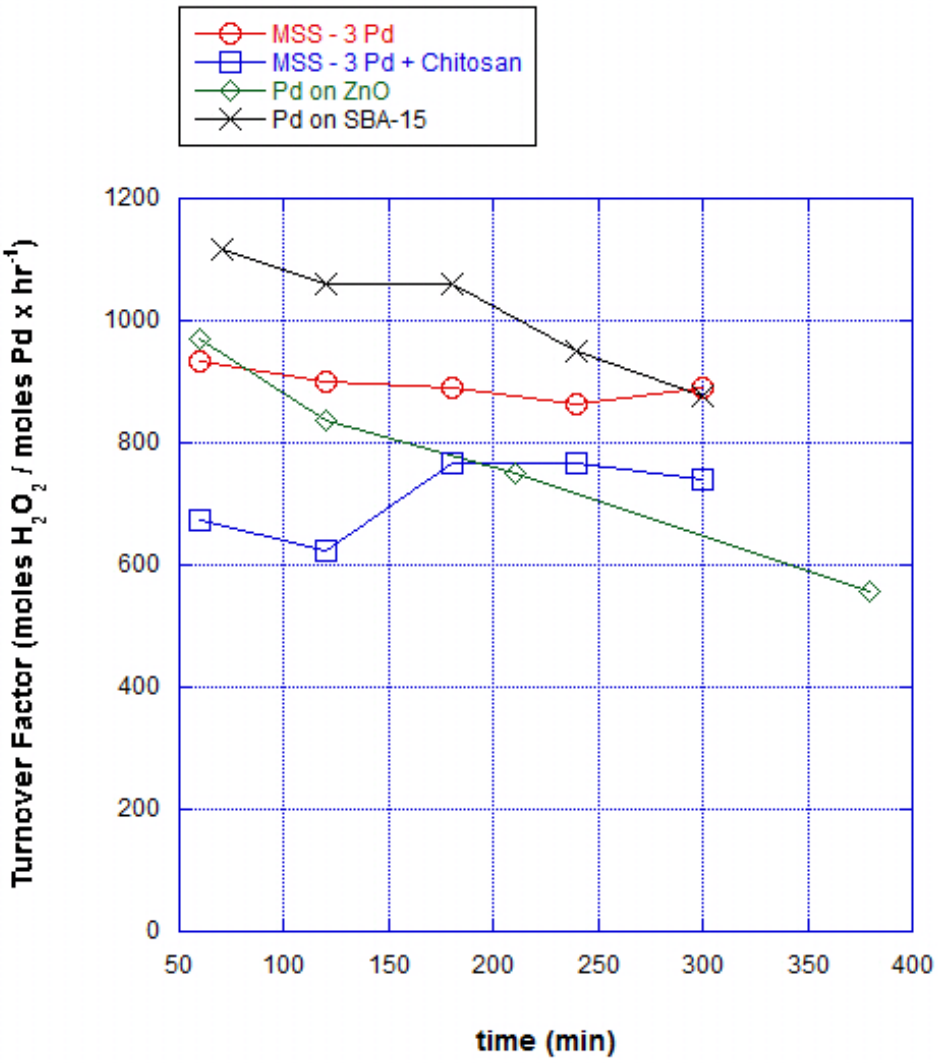

Figure 8: Performance of a Variety of Palladium-Containing Heterogeneous Catalysts for the Production of Hydrogen Peroxide

Samples prepared containing chitosan show a significant induction period, during which the catalytic performance may suffer from blockage of the palladium surface active sites. Due to the aqueous nature of the reaction conditions and chitosan's strong solubility in water, it makes sense that the catalyst performance improves as the contact time between catalyst and solvent is increased. The turnover frequency of the chitosan-containing sample never reaches the activity of the chitosan-free sample. This may be due to the blockage of some silica mesopores entirely by the large molecular weight polymer or by the non-reversible binding of the polymer's amine linkages to surface palladium atoms.

The non-porous zinc oxide particles showed strong initial catalytic activity, but exhibit a strong leaching of palladium into the reaction solution. This can be understood as the initial availability of active sites to hydrogen and oxygen, since the palladium particles are on the exposed surface of the nanoparticle scaffolds. Without the increased contact area between the palladium particle and a mesoporous host, the catalyst rapidly loses activity as it leaches palladium into solution.

Zinc oxide and palladium have been shown to form interfacial alloys, in which atoms of Pd from physisorbed Pd nanoparticles become alloyed into the ZnO surface through thermal treatment. These strongly bonded, highly active surfaces have shown excellent catalytic activity toward the steam reformation of methanol[55]. Two factors that may affect the poor catalytic performance of the Pd/ZnO system studied here are reduction temperature and surface morphology.

The temperature at which Pd/ZnO catalysts are reduced has been shown to have a great effect on the presence of Pd/Zn alloy, as studied by x-ray diffraction[56], with the alloy phase only beginning to form at temperatures of 623 K and above. The Pd/ZnO sample prepared by our group was reduced at a temperature of 473 K[48]. A recent study of ZnO single crystals showed that the (0001) crystalline surface is more likely to form Pd/Zn alloy, and is more catalytically active than the $(10\bar{1}0)$ surface[57]. Since the ZnO powder used to prepare our catalyst presents more than one crystalline surface, exact quantities unknown, it is possible that an unfavorable surface with decreased palladium−surface interactions is predominate.

The palladium-doped mesoporous silica spheres have shown continuous high turnover. While greater initial turnover frequencies are found in larger-pored silica (SBA-15) and nonporous zinc oxide scaffolds, these catalysts are found to lose activity over time due to the vulnerability of their catalysts to the reaction solution. By using a small pore with strong physisorption between the adsorbed palladium particle and substrate, the 3 nm pores strike a balance between availability of active sites to reactants and resistance to dissolution of the catalyst into solution. This balance allows the palladium-doped mesoporous silica spheres to maintain excellent activity toward the direct formation of hydrogen peroxide.

CHAPTER III

GRAPHENE-BASED MATERIALS FOR HYDROGEN STORAGE

The Rise of Graphene

Graphitic Materials Defined

Graphite, the most thermodynamically stable form of carbon, has a structure with layers of hexagonally-arranged carbon atoms. As shown in figure 9, the α form has alternating layers with atoms vertically aligned in every other layer. Interlayer spacing is 3.35 Å and corresponds to one-half of the *c* unit cell parameter[58]. Covalent bonding occurs only between carbon atoms of a single layer; interlayer bonding is weak and due only to van der Waals interactions. Slippage of these layers gives graphite its familiar lubricant properties.

The covalent bonding in graphite involves a conjugated network of sp^2-hybridized carbon atoms. These bonds are aromatic in nature, leading to a delocalization of electrons throughout the plane of carbon atoms. This delocalization gives graphite a metallic nature, allowing it to conduct electricity throughout the basal (001) plane, but not in other directions, where no covalent interactions exist.

If treated with strong oxidants, graphite may be oxidized to form graphite oxide. The aromatic carbon–carbon double bonds found in the basal plane of graphite are broken while carbon–oxygen bonds are formed above and below

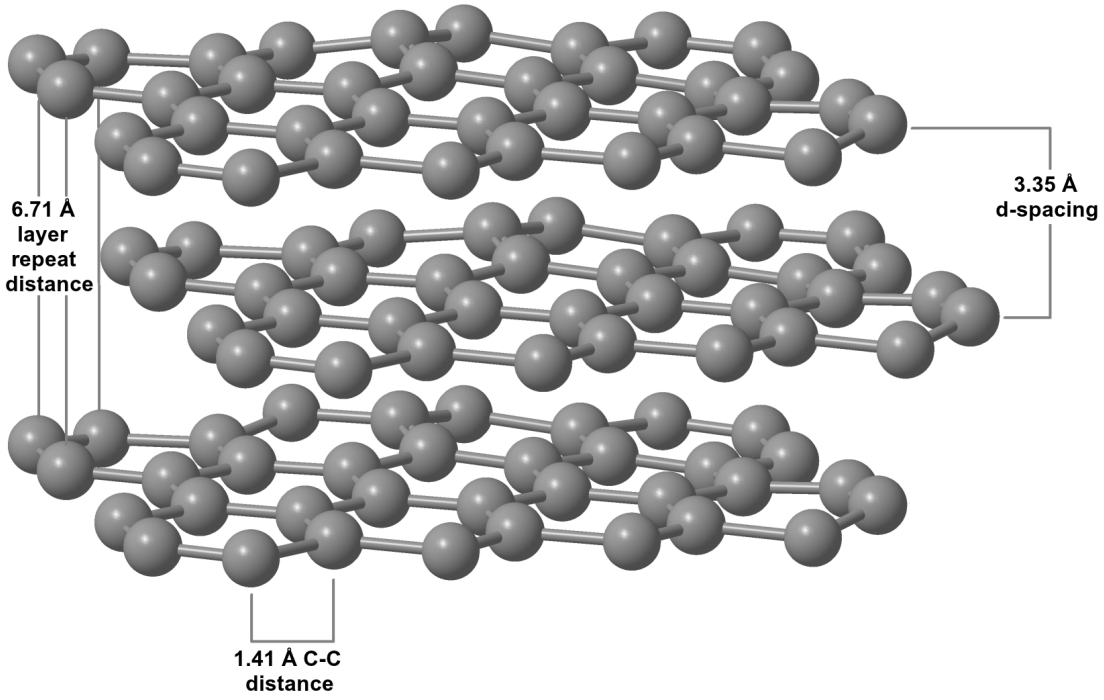

Figure 9: Structure of Hexagonal Graphite Showing the Alternating ABA Arrangement of Layers

each basal plane. The oxygen species attached to the graphitic carbons include hydroxyls, epoxides, and, at the edge of the graphite particle, carboxylic acids, esters, and ketones (figure 10)[59,60].

The oxidation of the sp^2-hybridized network has several ramifications for the bulk material. The formerly delocalized electrons are now covalently bonded to oxygen-containing groups, causing graphite oxide to be an insulator rather than a conductor in the basal plane, like graphite. The formation of the new sp^3-hybridized carbons also causes distortions in the flat (001) plane. Each of the reacted carbons attempts to form a tetrahedral environment, introducing strain into the sheet that manifests as deformations of the flat sheet into an irregularly curved surface. The distance between the sheets increases from the 3.35 Å found in graphite to greater than 6 Å, due to the presence of the interplanar functional groups as well as some amount of intercalated water[61].

By increasing the distance between the sheets through oxidation, the interactions between the sheets are significantly lessened. These oxidized sheets of graphite may be completely separated from one another much more readily than sheets of unreacted graphite. Whether separated by thermal or mechanical means, the individual sheets (or small groups of sheets) are sometimes given names in which "graphite" has been replaced with "graphene", such as "graphene oxide" [62], while the same material may also be called "graphite oxide sheets" [63] or "expanded graphite oxide" [64].

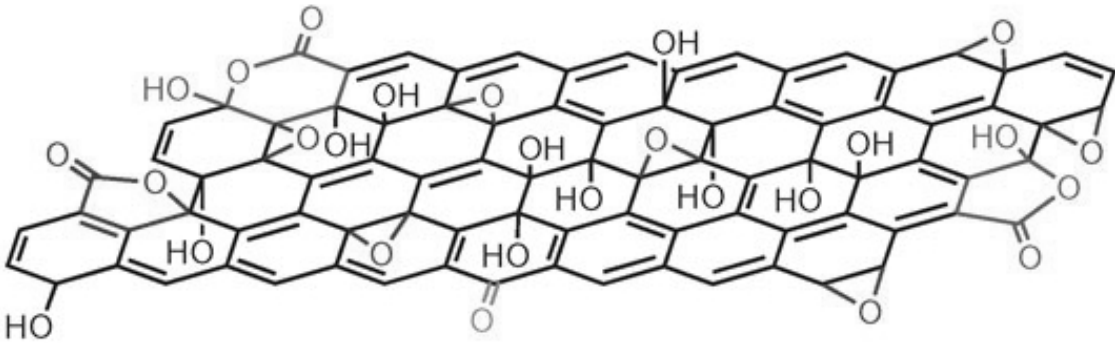

Figure 10: The Structure of Graphite Oxide as Determined by NMR[59].

The proper definition of graphene is of a two-dimensional, hexagonal array of sp^2-hybridized carbon atoms, which is identical to the (001) plane of hexagonal graphite. The material produced by the separation of layers of graphite oxide, on the other hand, is often quite different. Graphite oxide contains many domains of sp^3-hybridized carbons which remain after separation of the layers[59]. Complete separation of "graphite-based" materials into individual sheets of graphene is seldom achieved. Preparations described in the literature generally yield distributions of thicknesses of one to five layers of basal planes[64] while still receiving "graphene"-containing descriptions. Such ambiguities have resulted in materials that meet the proper definition of graphene often being referred to as "reduced graphene" [65] or "reduced graphene oxide" to emphasize that oxidized species are no longer present[62,66].

The thermal exfoliation process, during which samples of graphite oxide are rapidly heated to greater than 1000 °C, utilizes the violent evolution of gases from between the graphite oxide layers to force the layers apart. In a study of the gases released during thermal exfoliation, it has been found that vaporized water and carbon dioxide are evolved, with carbon dioxide being the major component. It is theorized that this evolved carbon dioxide results in vacancies within the resulting separated sheets[67].

Methods of Graphite Oxide Synthesis

The first reference to the oxidation of graphite appears to have come from Professor Brodie at the University of Oxford in 1859[68]. His work describes the treatment of graphite with many strong oxidants including sulfuric and nitric acids as well as potassium chlorate and dichromate to yield graphite oxide. He performed many further experiments on this product, including its heating to an unspecified temperature, at which time he made the following observation:

> *"when heated it undergoes a remarkable change; gases are given off in the interior of the substance, which swells up in a most singular manner and is reduced to the minutest state of division."*

It seems clear today that what Brodie observed was the formation of thermally exfoliated graphene oxide and that the gases given off were steam and CO_2, formed by the rapid volatilization of water trapped between the graphitic planes and the decomposition of oxidized graphite, respectively. The rapid escape of these gases cause the separation of lamellar planes, yielding individual sheets of oxidized graphene.

Brodie's method of oxidation involves the addition of potassium chlorate over the course of one week to a chilled solution of fuming nitric acid, resulting in the release of exceedingly hazardous chlorine dioxide gas. In 1958, Hummers and Offeman developed a process for the oxidation of graphite that is more reliably safe than the methods described by Brodie and results in the laboratory-scale production of graphite oxide over the course of a few hours[69]. Their method

uses sulfuric acid, sodium nitrate, and potassium permanganate to more safely oxidize graphite. Their improved method was proved invaluable half a century later. As interest in graphene-based materials increases exponentially in the twenty-first century, their contribution to the field continues to play a central role in its production. As of 2012, their single-page paper has surpassed 2,000 citations, and the "Hummers' Method" is part of the vernacular amongst scientist in the field.

Electronic Properties of Graphene and the Nobel Prize

In 2004 and 2005, Andre Geim, Konstantin Novoselov, and coworkers published the first electrical measurements on isolated graphene sheets. Their isolation of an individual graphene sheet was accomplished through the simple use of adhesive tape to separate the layers of highly-ordered pyrolytic graphite into individual sheets. Their real advancement was not in their synthetic technique, but in their ability to make the first electrical measurements of the micron-sized flake[70]. They showed the first evidence of graphene's unprecedented electron mobility and its stability as a 2D crystalline structure. This initial publication has led to an avalanche of research in the field, and was the first of many discoveries of the material's extraordinary properties, including tensile strength, stiffness, and thermal conductivity[71]. For their contribution to the field, the pair of researchers at Manchester University were awarded the 2010 Nobel Prize in Physics.

Motivation: LiO-Doped Pillared Graphene

A paper published in the Journal of Physical Chemistry Letters in 2010 by George Froudakis and his computational group at the University of Crete describes the study of a lithium-doped carbon structure designed to meet the US DOE hydrogen storage requirements[72]. The carbon substrate that the group used is theoretical in nature. The three-dimensional structure combines individual graphene sheets held parallel to one another by perpendicular "pillars" of single-wall carbon nanotubes which are fused to the graphene sheets[73]. To improve the interaction of this material with molecular hydrogen, the group introduced a dopant of LiO into their theoretical carbon scaffold, which yielded the desired result. Simulations showed that the material would surpass both the gravimetric and volumetric targets set by the Department of Energy for 2010 due to strong interactions between the lithium atom and gaseous hydrogen molecules.

While the material described in the paper is unlikely to ever be prepared *ex silico*, it does serve as a useful analogue for other graphene-based materials. The separation between graphene sheets described in the paper was varied from 11 to 36 Å, which are realistic values for graphite intercalation compounds. The dopant, LiO, was chosen to mimic the preparation of lithium-substituted hydroxyls on a carbon surface. Rather than create an sp^3-hybridized carbon material with surface hydroxyls (such as graphene oxide), the group simplified their task by using sp^2-hybridized nanotubes and sheets. When the LiO radical is placed near

the surface, the reactive oxygen chemisorbs to a carbon atom, creating a covalent bond similar to what would be found in a graphene oxide-based material in which surface hydroxyls were replaced by –OLi groups.

As eluded to in the journal article[72], the preparation of analogous compounds is a feasible synthetic goal. While the tuning of interlayer spacing may require advanced synthetic techniques, the modification of surface hydroxyls to create –OLi functional groups on a graphene oxide surface should be achievable by standard organometallic methodologies. It is the goal of this portion of the dissertation to show the preparation and analysis of just such a material. While individual sheets of lithium-functionalized graphene oxide are not expected to mimic the overall storage capacity of the theoretical porous material described by Froudakis, *et al.,* it may prove to have an increased storage capacity in comparison to unmodified graphene oxide, thereby lending some weight to the potential applicability of this class of materials for hydrogen storage.

Synthesis of Thermally Exfoliated Graphene Oxide and Lithium-Functionalized Graphene Oxide

Modification of the Hummers Method

Graphite oxide was prepared via a modified version of Hummers' Method of 1958[69]. Concentrated sulfuric acid (150 mL, Fisher, ACS grade) was chilled to 3 °C in a water-jacketed 500 mL round-bottom flask through the use of a closed-

cycle water chiller/recirculator. This setup allows for the maintenance of low temperatures throughout the following additions, despite the fact that many of them are strongly exothermic. An overhead stirrer was used for agitation of the prepared mixture with glass stirring rod and Teflon paddle.

Inside of a fume hood, 50 mL of 30% H_2O_2 in water (Fisher) was slowly added to the chilled sulfuric acid to create "piranha solution", which can be used to clean organic matter from inorganic substrates. Into this solution, 5.0 g graphite flake (Alfa Aesar, 7 - 10 micron, 99%) was dispersed and stirred for one hour to remove any adsorbed impurities from the graphite. The mixture was then slowly diluted with 350 mL of cold, deionized water.

The dilute mixture was next filtered through a 100 mL ground glass frit (Aldrich, medium) with the assistance of a diaphragm pump. Graphite collected atop the frit was washed with 1000 mL of deionized water and allowed to air dry before further use. After this cleaning process, the graphite displayed a near metallic luster, in stark comparison to the dull gray starting material.

The clean, dried graphite was dispersed with vigorous stirring into a chilled solution containing 200 mL of sulfuric acid and 5.0 g sodium nitrate (Fisher, granular, ACS grade). Into this mixture, 30 g of finely pulverized potassium permanganate (Acros, 98%) was added in small portions over a twenty minute period, causing the contents of the flask to become dark green in color. This mixture was allowed to warm to room temperature (the chiller was turned off) and was stirred for 15 hours (overnight).

The following day, the mixture was transfered into a 1 L beaker to allow for heating. The mixture was heated to 80 °C over a 15 minute period in an oil bath within a fume hood, resulting in a color change of the mixture to dark brown. To the warm, but cooling, mixture, 3% H_2O_2 (Fisher) was added dropwise until a bright yellow or orange color persisted (roughly 25 mL). The suspension was allowed to settle to the bottom of the beaker over several hours and was decanted to remove clear liquid from atop the solid particles.

The remaining slurry was then cleaned by centrifugation. In 25 mL centrifuge tubes, orange-brown solid material was separated from clear liquid at 30,000 rpm over 30 minutes. The liquid was decanted, discarded, and replaced by ~20 mL of deionized water. The solid was then re-suspended in the water using a mild ultrasonic bath for 60 minutes, before again undergoing centrifugation. This process was repeated three times to ensure that any soluble reactant ions were washed from the material.

The resulting graphite oxide, a brown, sticky material, was then transferred onto a large watch glass and placed inside an evacuated desiccator charged with ~ 20 g of anhydrous P_2O_5. As the desiccant removed water from the material, it was replaced with fresh P_2O_5. The sample was dried until it showed no sign of residual water (several days) before further use.

The dried graphite oxide is a brownish-black solid. The material maintains the shape and thickness in which it was applied to the watch glass before drying. Thicker pieces are near black in color and rigid to the touch while areas where it

was spread thin while still moist are lighter brown and quite pliable. The material may be broken into small pieces, but resists being ground into a powder. These characteristics suggest the presence of residual water intercalated between the layers, as described in the literature[67]. If force is exerted onto a small piece of graphite oxide with mortar and pestle, it may ignite, causing a small ember with a concussive evolution of smoke. This surprising result suggests the energetics of the material and the ease with which the material may be separated from one another.

Thermal Exfoliation

0.25 g dried graphite oxide was placed in an alumina tube, 25 mm in diameter and 60 cm in length. A quartz wool placed within the open end of the tube, then an o-ring sealed cap was affixed to the top which was in turn connected to valves leading to vacuum and a tank of argon gas. The tube was evacuated and filled with argon three successive time to eliminate oxygen. The valve leading to vacuum was replaced with 1/4” tubing leading to an oil bubbler. The argon valve was kept in place, but was closed. A Lindberg tube furnace was preheated to 1050 °C. The alumina tube, filled with argon over dried graphite oxide, was placed into the furnace and allowed to vent any escaping gases. Within moments of insertion into the furnace, the graphite oxide had expanded to form a voluminous, black solid that filled the inside of the alumina tube. This

expansion was accompanied by a violent evolution of gases through the oil bubbler.

The tube was removed from the furnace immediately after the reaction, no more than 10 seconds. After removal from the furnace, a light flow of argon was flowed through the tube and bubbler as it cooled to room temperature to avoid suck-back of oil into the sample tube. Once cool, the thermally exfoliated graphene oxide (TEGO) was removed from the tube and stored in a covered 1 L beaker in air.

A note of caution: the exfoliation process can be unexpectedly violent! The rapid evolution of gas should not be underestimated. Increases in the mass of starting graphite oxide should not be considered unless a larger tube and greater ability to vent the exiting gases are also put into place. 0.25 g of graphite oxide is the absolute maximum that should be used with the setup described above.

Functionalization of TEGO

The modification of graphene oxide material was accomplished by metalation of surface hydroxyl groups with an organolithium reagent in an inert atmosphere. 0.100 g of TEGO was heated under vacuum to 75 °C for 2 hours to remove any residual water. Higher temperatures were not used to avoid loss of any surface hydroxyl groups. To remove any trace amounts of water, pentane was dried over 4 Å molecular sieves, then distilled over sodium-potassium alloy

(NaK) within an atmosphere of argon using a Schlenk manifold to ensure the exclusion of air.

To 0.100 g of dried TEGO and a Teflon-coated stir bar within a 250 mL round-bottom Schlenk flask, 100 mL of dried pentane was transferred via stainless steel cannula under force of argon. Into this stirring mixture, 1.60 mL of 1.6 M *n*-butyllithium solution in hexanes (Aldrich) was injected via syringe. The mixture was stirred 15 hours before solvent was removed through the use of a glass filter-covered cannula. The black, solid product was further dried under dynamic vacuum.

Material Characterization

XRD

X-ray powder diffraction patterns of as-received graphite, prepared TEGO, and fully reduced graphene were all recorded using the Larese group instrument described herein. The lithium-functionalized TEGO pattern was recorded on the departmental PANalytical diffractometer.

Figure 10 shows the powder diffraction pattern of the as-received graphite flake. The pattern displays much greater signal to noise than the oxidized materials, suggesting its comparatively high degree of order. The most prominent of Miller indices are labeled. The most prominent peak, labeled (002) at 26 °2θ, corresponds to the repeating distance between identical basal planes. This

distance, 6.71 Å, is twice the distance of nearest neighbor planes, which are separated by 3.35 Å.

The XRD pattern obtained from a TEGO sample containing a small amount of graphite impurity is shown in figure 11. The pattern shows much lower resolution than graphite, suggesting the amorphous nature of the powder. Peaks at 26 and 44 °2θ roughly correspond to the (002) and (101) planes of graphite, while the broad feature centered near 18 °2θ represents an inter-layer repeat distance of 9.8 Å.

Graphene oxide that has been reduced to graphene yields an interesting diffraction pattern. Prepared by thermal treatment under a flow of 4% hydrogen gas, graphene sheets lack the strong hydrogen bonding interactions present in graphene oxide. The diffraction pattern shown in figure 10 contains no significant diffraction peaks greater than background scatter, suggesting that all inter-layer order has been destructed.

The XRD pattern of lithium-functionalized TEGO, coined “Lith-O-Graph”, is shown in figure 13. In an analogous fashion to pure graphene, it shows no strong diffraction peaks, suggesting the disruption of any inter-layer attractions that were present in graphene oxide.

Raman Spectroscopy

The Raman spectra were compared between graphite, TEGO, and Lith-O-Graph. The spectrum of graphite, figure 14, shows the characteristically strong G

band, which corresponds to vibrational modes along the *c*-axis of graphitic materials. The TEGO spectrum, as seen in figure 15, shows a much lower G band. Compared to graphite, the TEGO vibrational spectrum is much more heavily dominated by the D band, which is associated with edges and defects within the basal plane. This suggests that the TEGO particles are far more two-dimensional than the graphite precursor from which they were created[74]. The Raman spectrum of Lith-O-Graph, figure 16, similarly shows a high D to G band ratio. The ratio of intensities is clearly higher than in TEGO, suggesting, in agreement with XRD data, that the material is even more two-dimensional in nature than its hydroxylated precursor.

SSNMR

Solid-state NMR can be used to determine the functional groups found on graphite oxide. Using ^{1}H cross-polarization techniques, it has been shown[60] that peaks in the ^{13}C spectrum may be assigned to epoxy, hydroxyl, aliphatic, and ketyl groups. The ^{13}C spectrum of TEGO shown in figure 15 was recording using a magic angle spin rate of 5100Hz and a ^{1}H decoupled, ^{13}C direct pulse sequence. 8192 scans were recorded with a 5 second recycle delay. The presence of peaks representing epoxy (60 ppm), hydroxyl (70 ppm), graphitic (111 ppm), aliphatic (130 ppm), carboxylic (161 ppm) and ketyl (181 ppm) groups are consistent with oxidized graphene found elsewhere in the literature[59,61]. ^{6}Li

SSNMR spectra were also recorded for Lith-O-Graph, and show one single lithium environment, in agreement with the Li 1s XPS results.

XPS

XPS spectra were analyzed using Thermo Scientific Avantage software, which assigns and integrates peaks and calculates atomic weighting factors, allowing the percent surface composition of a material to be determined. The C 1s spectrum of Lith-O-Graph shows overlapping peaks corresponding to at least four distinct carbon atom environments, as measured by binding energies (figure 18). Peak centers are observed at 284.2, 284.9, 286.0, and 288.9 eV and are assigned as sp^2, sp^3, C–O, and carboxyl, respectively[75,76]. Total composition of carbon atoms at the surface were found to be 63.95% of all atoms. By mass, carbon was found to account for 62.6% of all atoms near the surface of the material.

The O 1s spectrum of Lith-O-Graph (figure 19) was found to contain three overlapping peaks. Peaks were found at 530.7, 531.7, and 533.0. W While the peak centered at 533.0 eV may be assigned as hydroxyl and ether groups[77], the two peaks lowest in energy may be assigned to the two oxygen environments present in carboxyl groups[78] C=O(OH) and C=O(OH), but also likely contains oxygen atoms bound to Li[79]. Oxygen atoms bound to lithium should have a lowered binding energy, since electropositive lithium should donate significant electron density to the oxygen to which it is bound. This increased valence

electron density causes shielding between the O 1s photoelectron and its nucleus, thus reducing the energy required for ejection of the photoelectron. Oxygen was found to make up 22.07% of all atoms near the surface of Lith-O-Graph and 28.8% by mass.

The Li 1s XPS spectrum (figure 20) was found to contain only one symmetric peak, centered at 54.8 eV, which shows that lithium is present in only one chemical environment. The integration of this peak suggests that lithium makes up 13.58% of the atoms at the surface of Lith-O-Graph, but only 7.68% by mass due to its low atomic weight. Less than 0.4% of the surface was found to contain any contaminating atoms, with sulfur (0.3%) and fluorine (<0.1%) combining to make up the only measurable impurities.

TEM

TEM images provide information about the quality of the graphitic substrates prepared. Images of bare TEGO show the material to be clearly three layers thick, by examination of the edges of some nanoparticles (figure 19), but of greater, indeterminate thickness in other particles (figure 20). Figure 20 also shows the presence of some heavier atoms (bright spots) on the surface of TEGO.

Images of Lith-O-Graph show varying thickness of material by lighter areas (thicker) and darker areas (thinner) across the surface of the material

(figure 21). Also present are some heavier, contaminating atoms seen as bright spots in the image. Individual lithium and oxygen atoms are below the instrument's resolution, and could not be detected. No areas of sintered lithium deposits were found, suggesting that any lithium atoms in the material must be individually bound to the surface.

Hydrogen Adsorption Isotherms

While it has been theorized that Lith-O-Graph would hold increased affinity for hydrogen when compared to TEGO, initial experiments have shown the opposite to be true. Figure 22 shows a comparison of hydrogen adsorption isotherms performed at 15 K. Lith-O-Graph shows only 30% of the hydrogen monolayer capacity of TEGO per gram of material.

Considerations for Modifications and Improvement

Modification of the material to better mimic the pillared graphene structure might improve the storage capacity of lithium-functionalized graphitic materials. The addition of linker molecules between graphene sheets to create tunable interlayer spacing would be an ambitious undertaking, but porous graphene, carbon-based aerogels, and other high surface area, porous materials currently under development would likely offer improved hydrogen storage capabilities.

The role of lithium oxide in aiding in those storage capabilities has yet to be proven.

CHAPTER IV

CONCLUSION

Mesoporous silica particles were prepared following standard methodology and analyzed by electron microscopy and SAXS. SEM images have shown the material produced to be roughly spherical, with particle diameters in the range of 300 to 500 nm. SAXS measurements confirm the predicted hexagonal array of mesopores, with pore centers separated by 3.3 nm. This material was impregnated with palladium nanoparticles which proved to create an efficient heterogeneous catalysts for the direct formation of hydrogen peroxide. The catalyst proved more robust than similar catalysts due to a believed strong interaction between the palladium nanoparticles and the mesopores of the silica substrate. Chitosan, a bio-polymer that has been shown to bind to palladium atoms, was deposited within the porous silica, but showed no benefit to the catalyst.

Graphite oxide, thermally exfoliated graphene oxide, and a lithium-functionalized graphene oxide material were all prepared and characterized. XRD and Raman spectroscopy gave results that were consistent with the separation of graphene sheets, while electron microscopy confirmed that the graphene materials were in fact only a few layers in thickness. XPS and SSNMR confirmed the presence of lithium within the lithium-functionalized samples, as well of the degrees to which the graphitic materials had been oxidized. XPS and

TEM also suggested a small amount of impurities on the material surfaces. Initial testing has shown that, despite efforts to recreate the theoretical materials described in the literature, Lith-O-Graph is a very poor hydrogen storage material at low temperatures.

LIST OF REFERENCES

(1) Cademartiri, L., Ozin, G. A., *Concepts of Nanochemistry*, Wiley-VCH: Weinheim, Germany, 2009.

(2) Li, Q., Kako, T., Ye, J., *J. Mater. Chem.*, **2010**, *20*, 10187-92.

(3) Braga, A.,Giménez, S., Concina, I., Vomiero, A., Mora-Seró, I., *J. Phys. Chem. Lett.*, **2011**, *2*, 454-60.

(4) Tang, Z. K., Zhang, L., Wang, N., Zhang, X. X., Wen, G. H., Li, G. D., Wang, J. N., Chan, C. T., Sheng, P., *Science*, **2001**, *292*, 2462-5.

(5) Lai, C.-Y., Trewyn, B. G., Jeftinija, D. M., Jeftinija, K., Xu, S., Jeftinija, S., Lin, V. S.-Y., *J. Am. Chem. Soc.*, **2003**, *125*, 4451-9.

(6) Huang, X., El-Sayed, I. H., Qian, W., El-Sayed, M. A., *J. Am. Chem. Soc.*, **2006**, *128*, 2115-20.

(7) Machida, M., Murakami, K., Hinokuma, S., Uemura, K., Ikeue, K., Matsuda, M., Chai, M., Nakahara, Y., Sato, T., *Chem. Mater.*, **2009**, *21*, 1796-8.

(8) Qi, L., Sorge, J. D., Birnie III, D. P., *J. Am. Ceram. Soc.*, **2009**, *92*, 1921-5.

(9) Nadj-Perge, S., Frolov, S. M., Bakkers, E. P. A. M., Kouwenhoven, L. P., *Nature*, **2010**, *468*, 1084–7.

(10) Xuan, Y., Wu, Y. Q., Shen, T., Qi, M., Capano, M. A., Cooper, J. A., Ye, P. D., *Appl. Phys. Lett.*, **2008**, *92*, 013101/1-013101/4.

(11) Blasko, T., Nieto, J. M. L., *Appl. Catal. A*, **1997**, *157*, 117-42.

(12) Thüne, P. C., Loos, J., Wouters, D., Lemstra, P. J., Niemantsverdriet, J. W., *Macromol. Symp.*, **2001**, *173*, 37-52.

(13) Galvis, H. M. T., Bitter, J. H., Khare, C. B., Ruitenbeek, M., Dugulan, A.I., de Jong, K. P., *Science*, **2012**, *335*, 835-8.

(14) Bell, A. T., *Science*, **2003**, *299*, 1688-91.

(15) United States Department of Energy, Office of Energy Efficiency and Renewable Energy, *Fuel Cell Technologies Program Multi-Year Research, Development and Demonstration Plan: Hydrogen Storage, 2011 Interim Update*, www1.eere.energy.gov/hydrogenandfuelcells/mypp/pdfs/storage.pdf (accessed April 2, **2012**).

(16) Cullity, B. D., Stock, S. R., *Elements of X-Ray Diffraction*, 3rd ed., Prentice Hall: Upper Saddle River, NJ, **2001**.

(17) Scherrer, P., *Nachr. Ges. Wiss. Göttingen*, **1918**, *26*, 98-100.

(18) Holzwarth, U., Gibson, N., *Nature Nanotech.*, **2011**, *6*, 534.

(19) Langford, J. I., Wilson, A. J. C., *J. Appl. Cryst.*, **1978**, *11*, 102-13.

(20) Borchert, H., Shevchenko, E. V., Robert, A., Mekis, I., Kornowski, A., Grübel, G., Weller, H., *Langmuir*, **2005**, *21*, 1931-6.

(21) Huo, Q., Margolese, D. I., Stucky, G. D., *Chem. Mater.*, **1996**, *8*, 1147-60.

(22) Kruk, M., Cao, L., *Langmuir*, **2007**, *23*, 7247-54.

(23) Wang, J., Li., F., Zhou, H., Sun, P., Ding, D., Chen, T., *Chem. Mater.*, **2009**, *21*, 612-20.

(24) Akitt, J. W., Mann, B. E., *NMR and Chemistry*, 4th ed., Stanley Thornes: Cheltenham, UK, **2000**.

(25) Iggo, J. A., *NMR Spectroscopy in Inorganic Chemistry*, Oxford: New York, **1999**.

(26) Blümich, B., ed., *Solid State NMR I Methods*, Springer-Verlag: Berlin, **1994**.

(27) Skoog, D. A., Holler, F. J., Nieman, T. A., *Principles of Instrumental Analysis*, 5th ed., Harcourt Brace: Philadelphia, **1998**.

(28) Harris, D. C., Bertolucci, M. D., *Symmetry and Spectroscopy*, Oxford: New York, **1978**.

(29) Watts, J. F., Wolstenholme, J., *An Introduction to Surface Analysis by XPS and AES*, Wiley: Chichester, UK, **2003**.

(30) Nellist, P. D., Chisholm, M. F., Dellby, N., Krivanek, O. L., Murfitt, M. F., Szilagyi, Z. S., Lupini, A. R., Borisevich, A., Sides, W. H. Jr., Pennycook, S. J., *Science*, **2004**, *305*, 1741.

(31) Mursic, Z., Lee, M. Y. M., Johnson, D. E., Larese, J. Z., *Rev. Sci. Instrum.*, **1996**, *67*, 1886-90.

(32) Kroschwitz, J. I., ed., *Kirk-Othmer Encyclopedia of Chemical Technology*, *Vol. 13*, 5th ed., Wiley: New York, **2005**.

(33) Shin, H., Sugano, J., Yoshii, T., Iwamoto, K., Kuriyama, Y., Kakuda, M., U.S. Pat. 3,965,251, **1976**, to Mitsubishi Gas Chemical Co.

(34) Sethi, D. S., U.S. Pat. 4,824,609, **1989**, to FMC Corp.

(35) Rushmere, J. D., U.S. Pat. 4,668,499, **1987**, to E. I. Du Pont de Nemours and Co.

(36) Pospelova, T. A., Kobozev, N. I., Eremin, E. N., *Rus. J. Phys. Chem.*, **1961**, *35*, 143.

(37) Burch, R., Ellis, P. R., *Appl. Catal. B: Environmental*, **2003**, *42*, 203-11.

(38) Han, Y., Lunsford, J. H., *J. Catal.*, **2005**, *230*, 313-6.

(39) Liu, Q., Lunsford, J. H., *Appl. Catal. A: General*, **2006**, *314*, 94-100.

(40) Liu, Q., Lunsford, J. H., *J. Catal.*, **2006**, *239*, 237-43.

(41) Yildiz, M., Akin, A. N., *Turk. J. Chem.*, **2007**, *31*, 479-86.

(42) Samanta, C., Choudhary, V. R., *Catal. Comm.*, **2007**, *8*, 2222-8.

(43) Ntainjua N, E., Edwards, J. K., Carley, A. F., Lopez-Sanchez, J. A., Moulijn, J. A., Herzing, A. A., Kiely, C. J., Hutchings, G. J., *Green Chem.*, **2008**, *10*, 1162-9.

(44) Liu, Q., Bauer, J. C., Schaak, R. E., Lunsford, J. H., *Angew.Chem. Int. Ed.*, **2008**, *47*, 6221-4.

(45) Edwards, J. K., Solsona, B., Ntainjua N, E., Carley, A. F., Herzing, A. A., Kiely, C. J., Hutchings, G. J., *Science*, **2009**, *323*, 1037-41.

(46) Chanaa, S. Z., *Materials Chemistry of Nanocubes and Mesoporous Silicas: Characterization and Adsorption Studies*, dissertation, Univ. Tenn., Knoxville, **2008**.

(47) Kresge, C. T., Leonowicz, M. E., Roth, W. J., Vartuli, J. C., Beck, J. S., *Nature*, **1992**, *359*, 710-2.

(48) Kumar, M. N. V. R., Muzzarelli, R. A. A., Muzzarelli, C., Sashiwa, H., Domb, A. J., *Chem. Rev.,* **2004,** *104*, 6017.

(49) Tong, J., Li, Z., Xia, C., *J. Mol. Catal. A: Chem.*, **2005**, *231*, 197-203.

(50) Hardy, J. J. E., Hubert, S., Macquarrie, D. J., Wilson, A. J., *Green Chem.,* **2004**, *6*, 53-6.

(51) Guzman, J., Saucedo, I., Navarro, R., Revilla, J., Guibal, E., *Langmuir* **2002**, *18*, 1567-73.

(52) Huang, M. H., Choudrey, A., Yang, P., *Chem. Comm.*, **2000**, *12*, 1063-4.

(53) Tun, Z., Mason, P. C., *Acta Cryst. A*, **2000**, *56*, 536-9.

(54) Smarlsy, B., Groenwolt, M., Antonietti, M., *Progr. Colloid Polym. Sci.*, **2005**, *130*, 105-13.

(55) Iwasa, N., Takezawa, N., *Top. Catal.*, **2003**, *22*, 215-24.

(56) Landry, P. E., *Adsorption of Hydrogen onto Bare and Metal Decorated Metal Oxides*, dissertation, Univ. Tenn., Knoxville, **2011**.

(57) Hyman, M. P., Lebarbier, V. M., Wang, Y., Datye, A. K., Vohs, J. M., *J. Phys. Chem. C,* **2009**, *113*, 7251-9.

(58) Greenwood, N. N., Earnshaw, A., Chemistry of the Elements, 2nd ed., Butterworth-Heinemann, Oxford, **1997**.

(59) Gao, W., Alemany, L. B., Ci, L., Ajayan, P. M., *Nature Chem.*, **2009**, *1*, 403-8,

(60) Lee, D. W., De Los Santos V., L., Seo, J. W., Leon Felix, L., Bustamante D., A., Cole, J. M., Barnes, C. H. W., *J. Phys. Chem. B*, **2010**, *114*, 5723-8.

(61) Stankovich, S., Dikin, D. A., Piner, R. D., Kohlhaas, K. A., Kleinhammes, A., Jia, Y., Wu, Y., Nguyen, S., T., Ruoff, R. S., *Carbon*, **2007**, *45*, 1558-65.

(62) Liu, S., Zeng, T. H., Hofmann, M., Burcombe, E., Wei, J., Jiang, R., Kong, J., Chen, Y., *ACS Nano*, **2011**, *5*, 6971-80.

(63) Kovtyukhova, N. I., Ollivier, P. J., Martin, B. R., Mallouck, T. E., Chizhik, S. A., Buzaneva, E. V., Gorchinskiy, A. D., *Chem. Mater.*, **1999**, *11*, 771-8.

(64) Wu, Z.-S., Ren, W., Gao, L., Liu, B., Jiang, C., Cheng, H.-M., *Carbon*, **2009**, *47*, 493-9.

(65) Tang, L., Wang, Y., Li, Y., Feng, H., Lu, J., *Adv. Func. Mat.*, **2009**, *19*, 2782-9.

(66) Park, S., An, J. H., Jung, I. W., Piner, R. D., An, S. J., Li, X. S., Velamakanni, A., Ruoff, R. S., *Nano Lett.*, **2009**, *9*, 1593-7.

(67) Schniepp, H. C., Li, J.-L., McAllister, M. J., Sai, H., Herrera-Alonso, M., Adamson, D. H., Prud'homme, R. K., Car, R., Saville, D. A., Aksay, I. A., *J. Phys. Chem. B*, **2006**, *110*, 8535-9.

(68) Brodie, B., *Phil. Trans. R. Soc. Lond.*, **1859**, *149*, 249-59.

(69) Hummers, Jr., W. S., Offeman, R. E., *J. Am. Chem. Soc.*, **1958**, *80*, 1339.

(70) Novoselov, K. S., Geim, A. K., Morozov, S. V., Jiang, D, Zhang, Y., Dubonos, S. V., Grigorieva, I. V., Firsov, A. A., *Science*, **2004**, *306*, 666-9.

(71) Savage, N., *Nature*, **2012**, *483*, S30-1.

(72) Tylianakis, E., Psofogiannakis, G. M., Froudakis, G. E., *J. Phys. Chem. Lett.*, **2010**, *1*, 2459-64.

(73) Dimitrakakis, G., Tylianakis, E., Froudakis, G., *Nano Lett.*, **2008**, *8*, 3166–70.

(74) Ferrari, A. C., Meyer, J. C., Scardaci, V., Casiraghi, C., Lazzeri, M., Mauri, F., Piscanec, S., Jiang, D., Novoselov, K. S., Roth, S., Geim, A. K., *Phys. Rev. Lett.*, **2006**, *97*, 187401.

(75) Perruchot, C., Watts, J. F., Lowe, C., White, R. G., Cumpson, P. J., *Surf. Interf. Anal.*, **2002**, *33*, 869-78.

(76) Moulder, J. F., Stickle, W. F., Sobol, P. E., Bomben, K., *Handbook of X-ray Photoelectron Spectroscopy*, Physical Electronics Inc., Eden Prairie, USA, **1992**.

(77) Lopez, G. P., Castner, D. G., Radner, B. D., *Surf. Interf. Anal.*, **1991**, *17*, 267-72.

(78) Alexander, M. R., Beamson, G., Blomfield, C. J., Leggett, G., Duc, T. M., *J. Electron Spec. and Relat. Phenom.*, **2001**, *121*, 19-32.

(79) Van der Heide, P., *X-ray Photoelectron Spectroscopy, an Introduction to Principles and Practices*, Wiley, Hoboken, USA, **2012**.

APPENDIX

Table 1: Lattice Parameters from SAXS Data for 2D Hexagonal Array of Mesopores in Silica Spheres

q ($Å^{-1}$)	*(hk)*	*d-spacing (Å)*	*a (Å)*
0.19	(10)	33	38
0.33	(11)	19	
0.38	(21)	17	

Table 2. ICP-OES Results of Pd Loading in Mesoporous Silica Spheres, both With and Without Chitosan

Sample #	*Mass of $Pd(OAc)_2$ added*	*Mass of Substrate*	*Calculated Weight % Pd*	*ICP-OES Measured Weight % Pd*
1-Pd	10.0 mg	368 mg	1.27%	2.100%
2-Pd	3.2 mg	86 mg	1.72%	1.568%
3-Pd	4.5 mg	98 mg	2.13%	1.816%
4-Chitosan-Pd	3.0 mg	95 mg	1.47%	1.133%

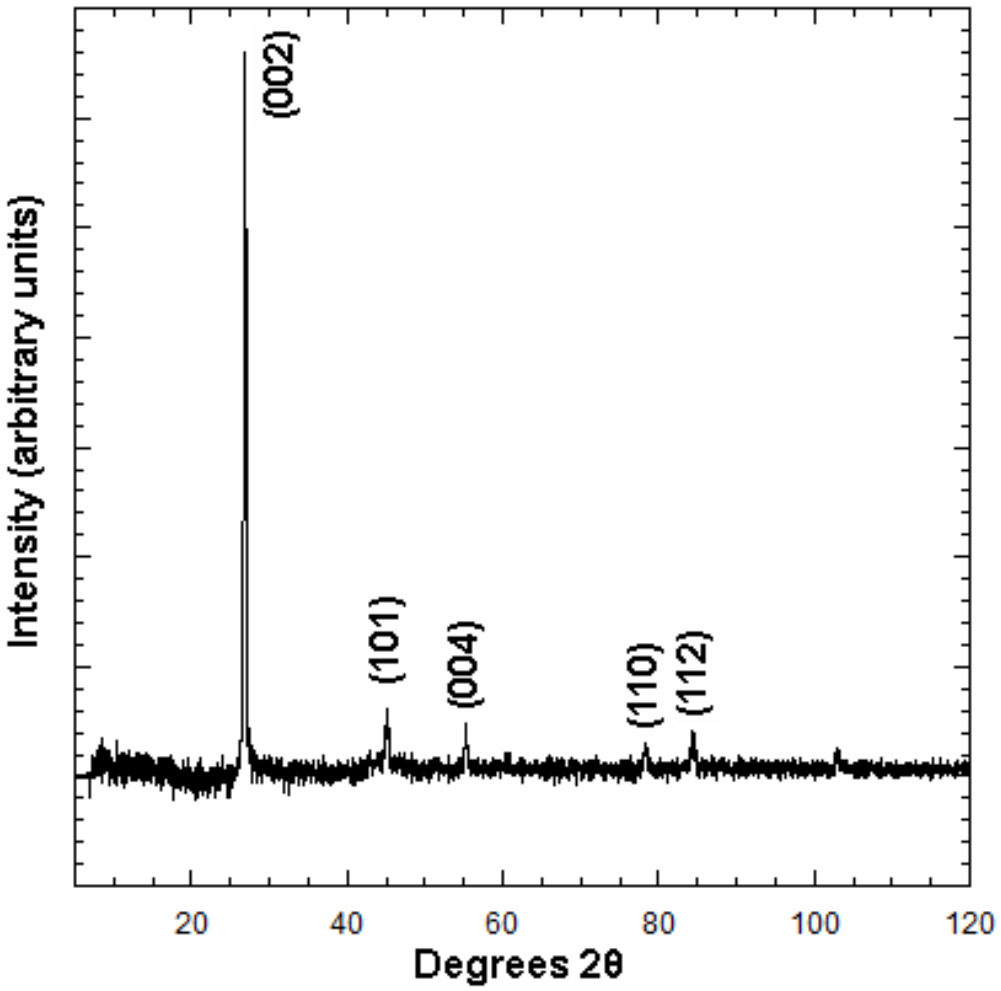

Figure 11: The XRD pattern of graphite starting material, labeled with Miller Indices

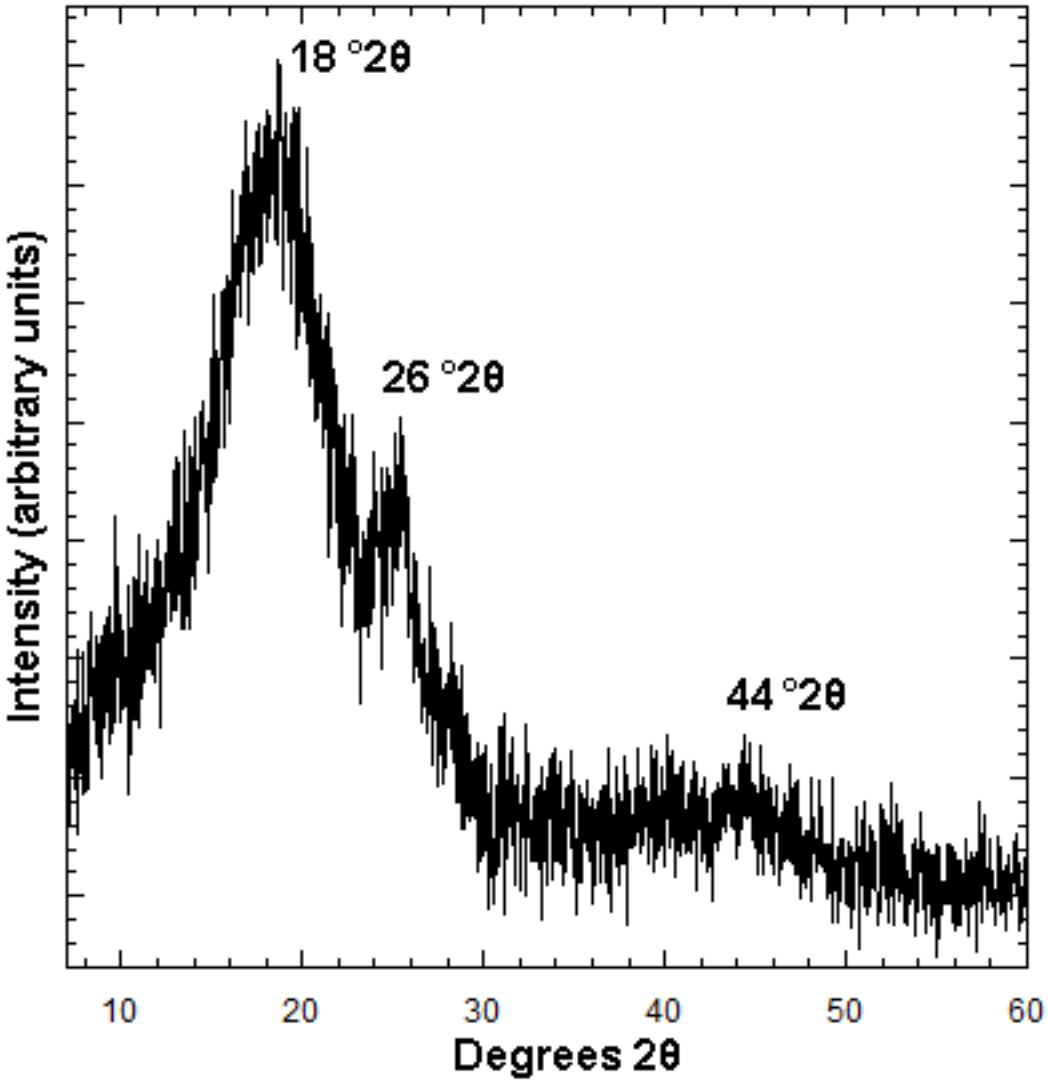

Figure 12: The XRD pattern of graphene oxide with graphite impurity at 26 and 44 °2θ

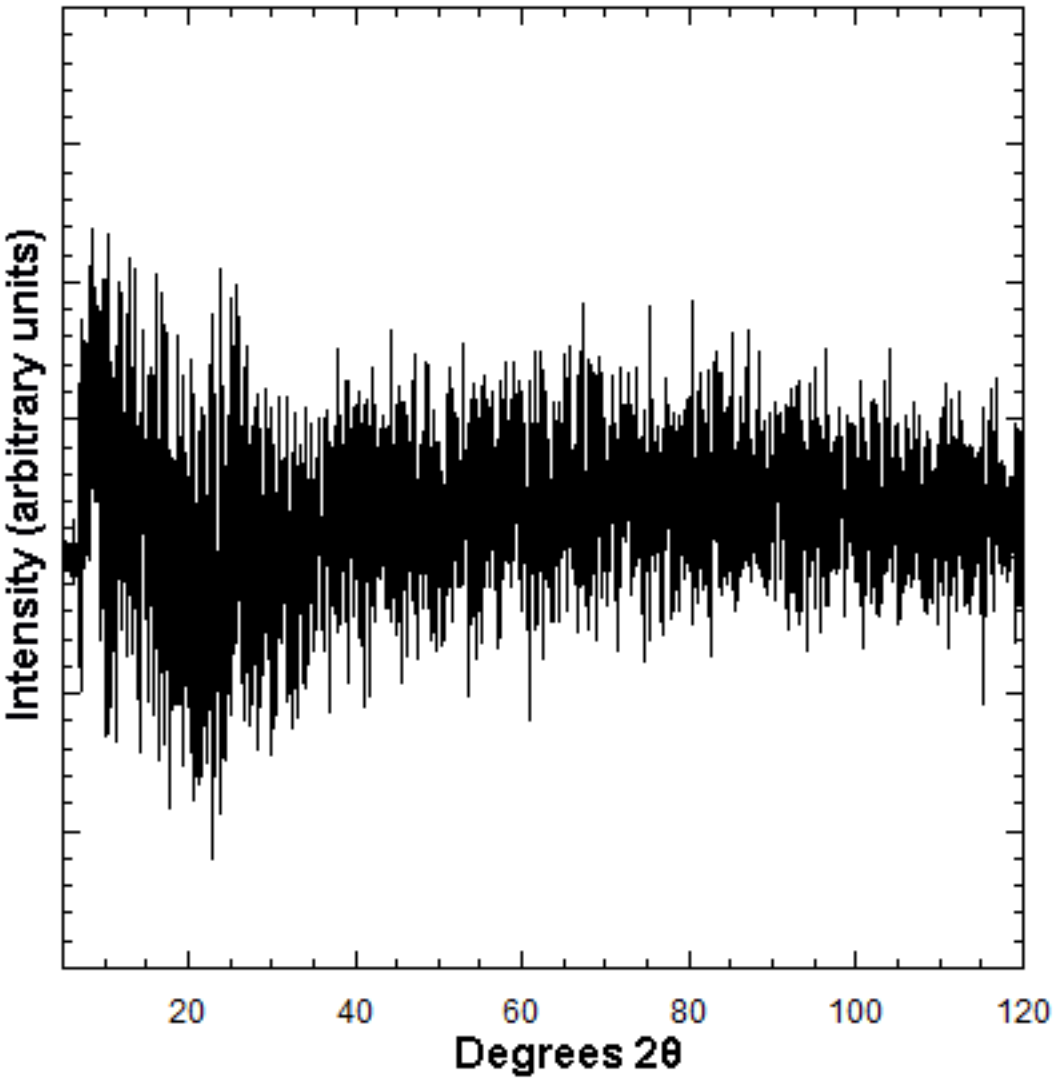

Figure 13: XRD pattern of reduced graphene, showing no diffraction peaks stronger than background scatter

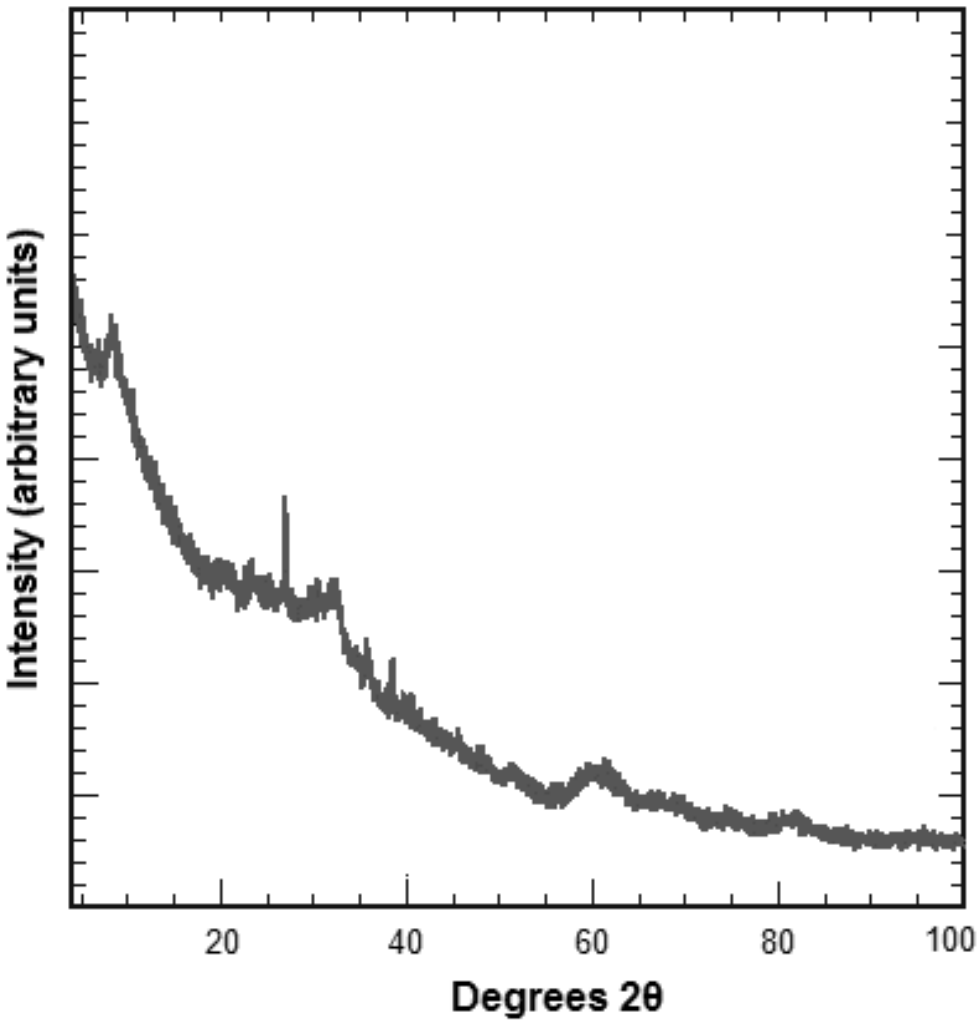

Figure 14: XRD pattern of Lith-O-Graph, showing no strong diffraction peaks

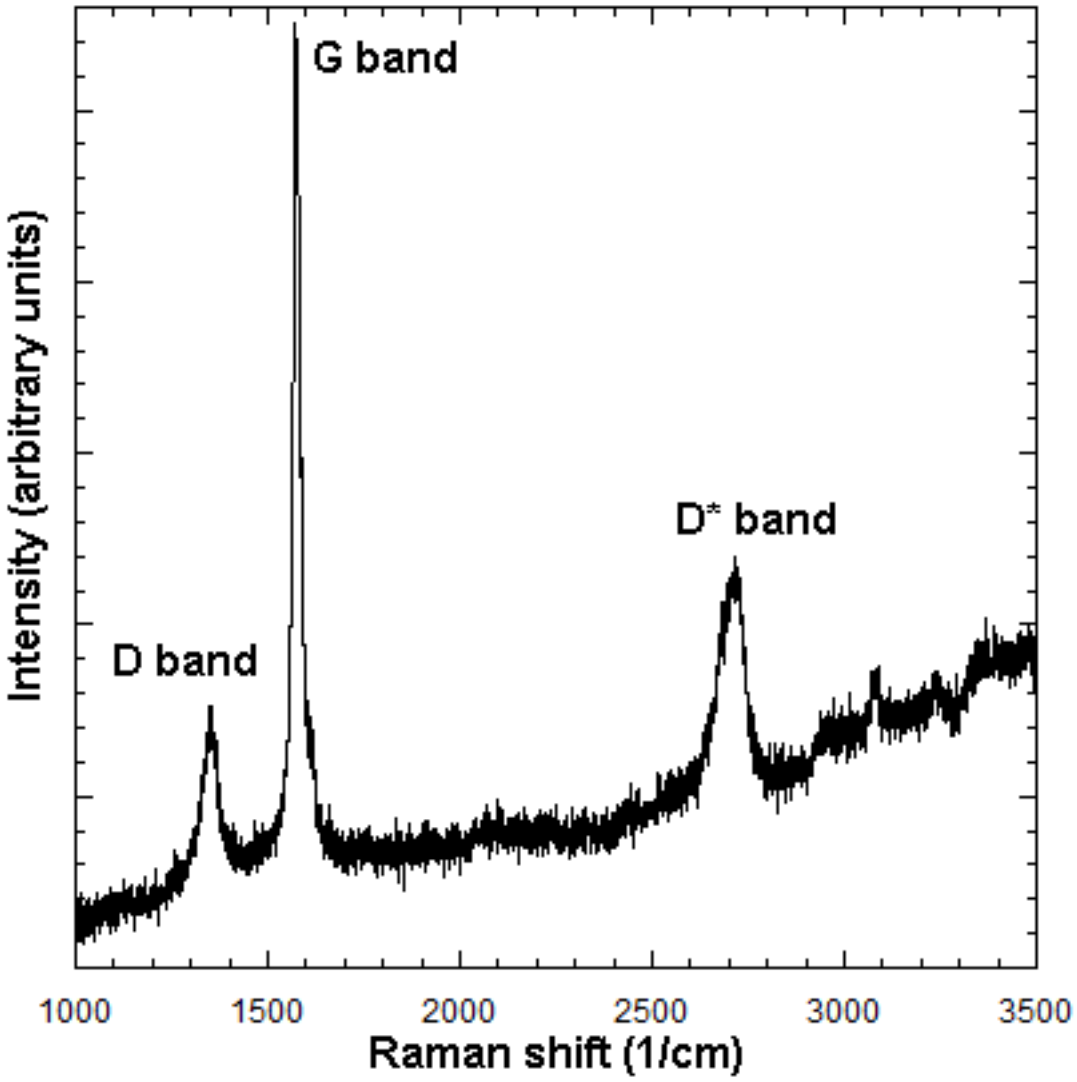

Figure 15: The Raman spectrum of as-received graphite shows a low D to G band ratio.

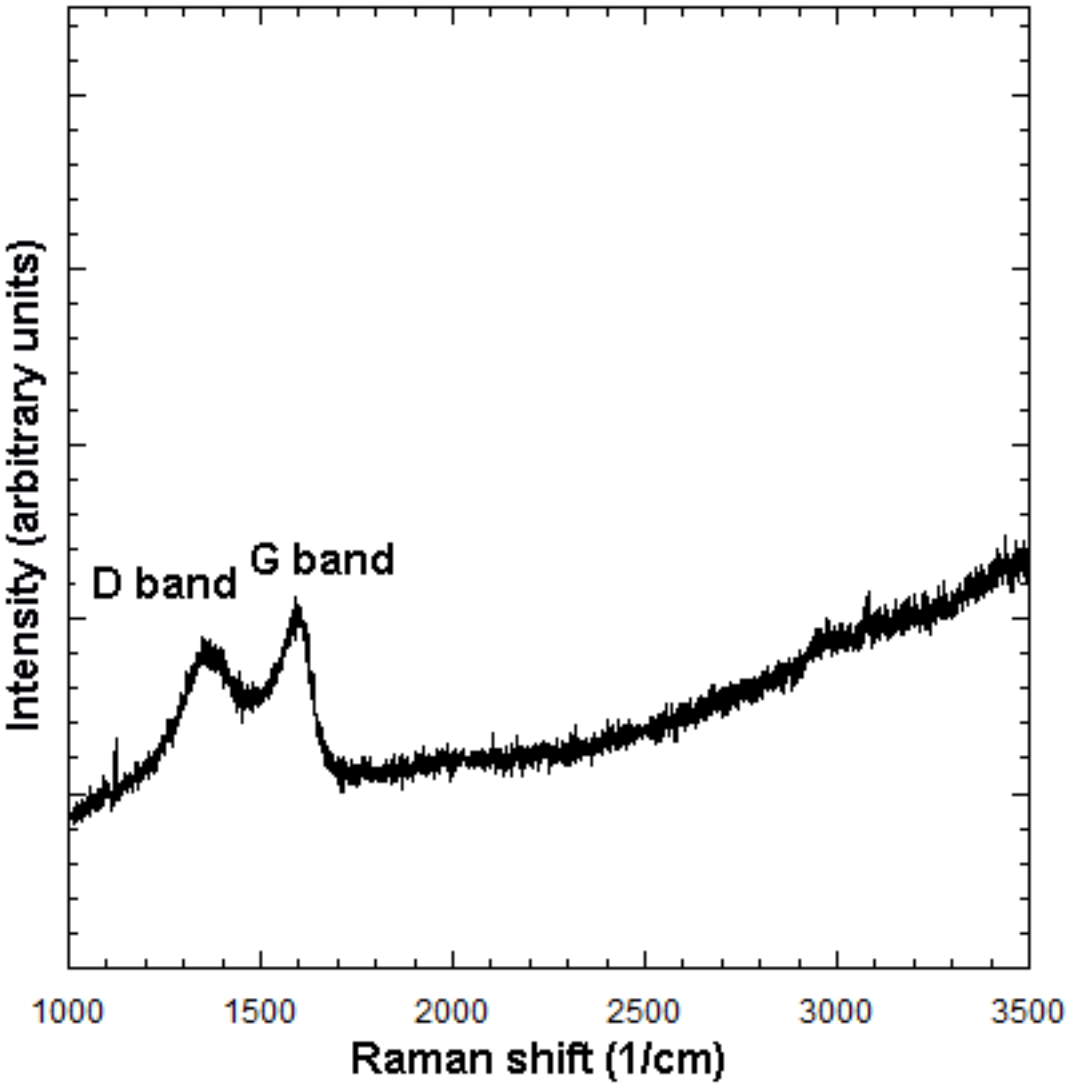

Figure 16: The Raman spectrum of TEGO shows a much higher D to G band ratio than graphite.

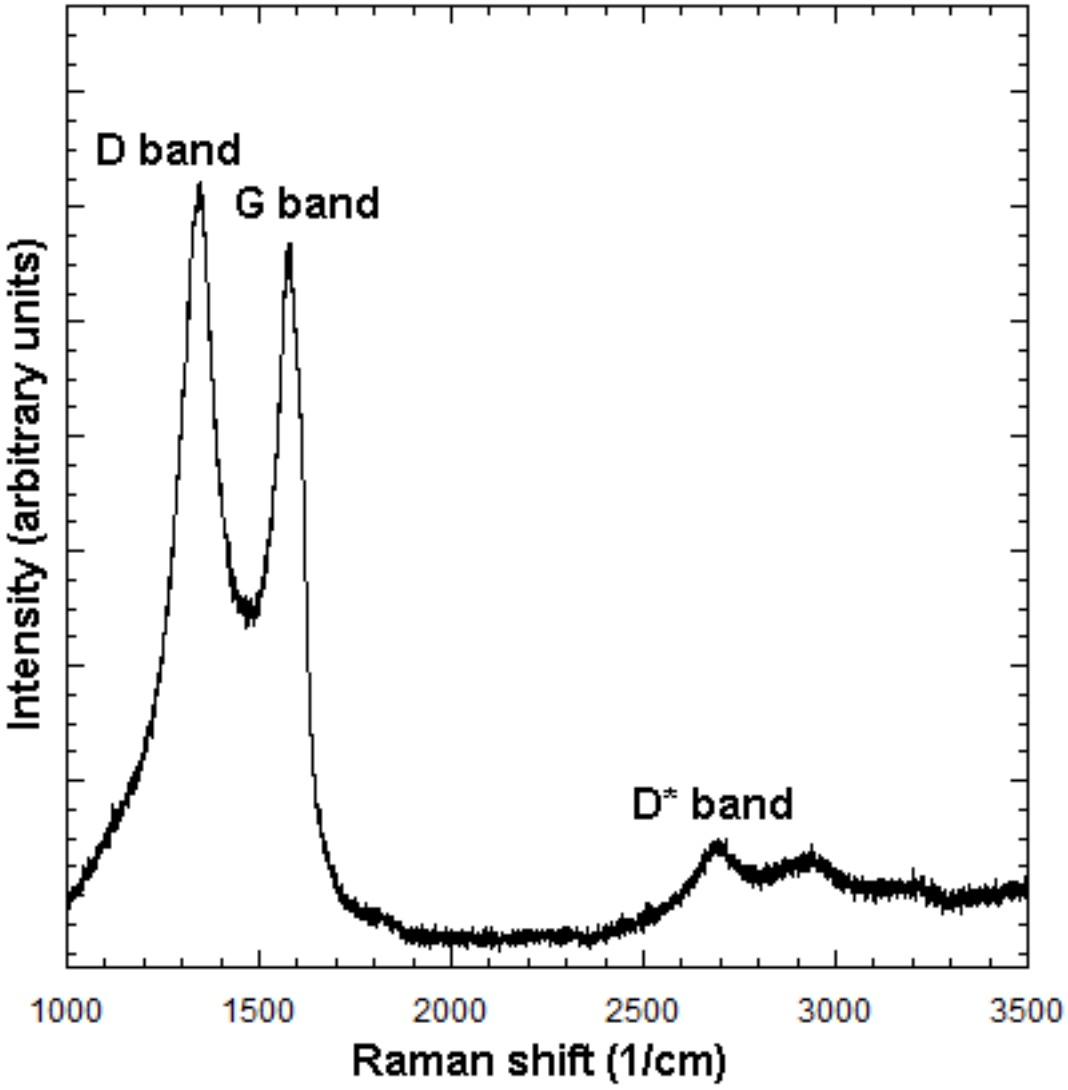

Figure 17: Raman spectrum of Lith-O-Graph shows a greater D to G band ratio than either TEGO or graphite.

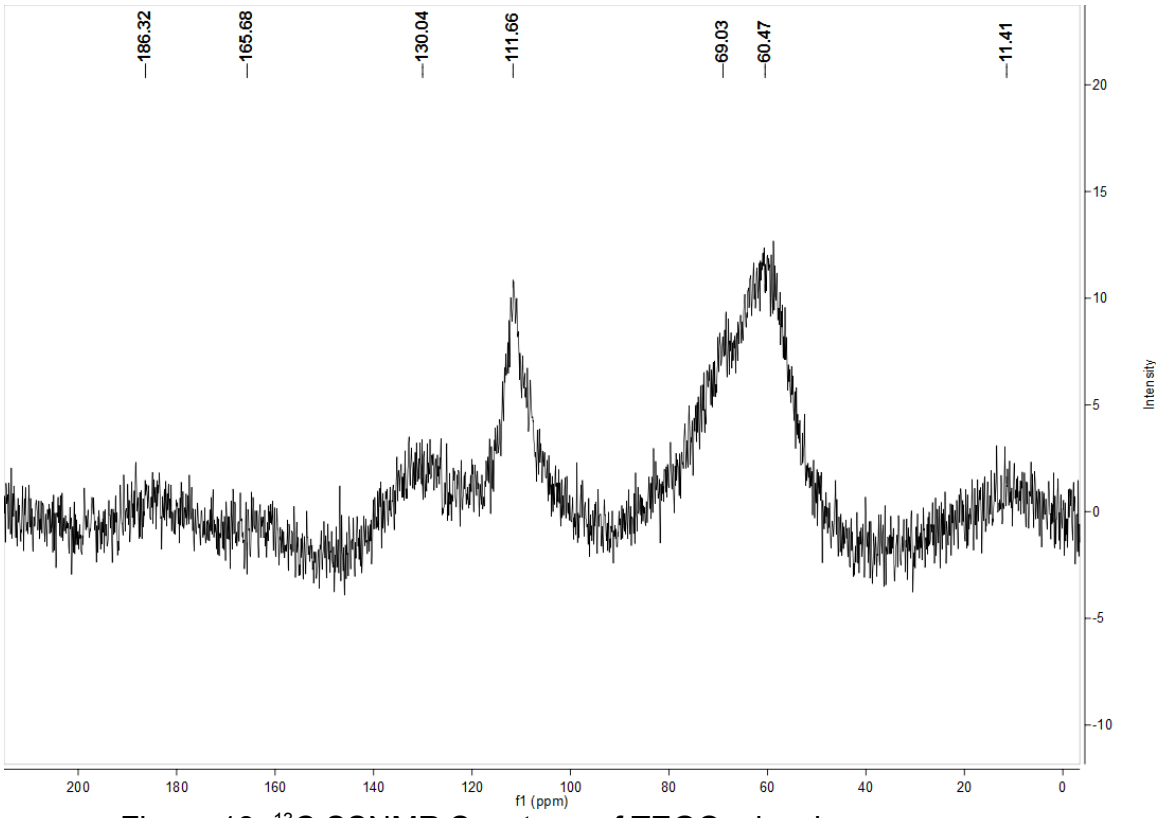

Figure 18: ^{13}C SSNMR Spectrum of TEGO, showing resonances corresponding to both oxidized and sp^2 carbon

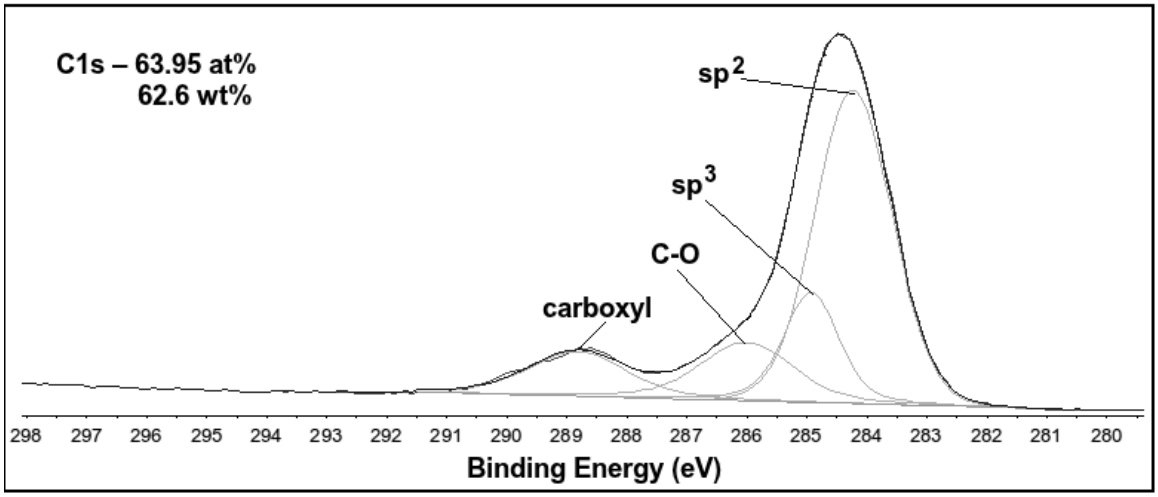

Figure 19: The C 1s XPS spectrum of Lith-O-Graph shows four distinct carbon environments

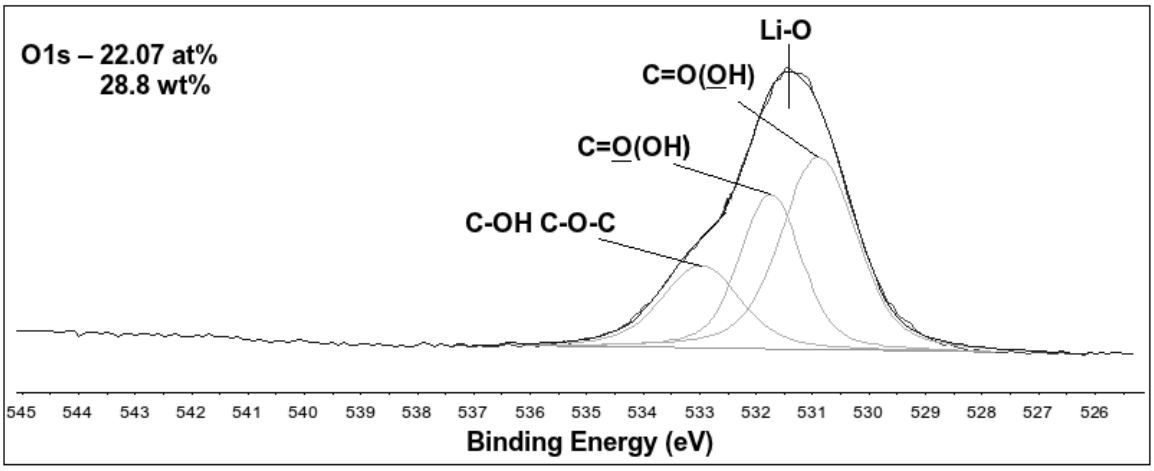

Figure 20: O 1s XPS spectrum of Lith-O-Graph shows multiple different oxygen environments are present

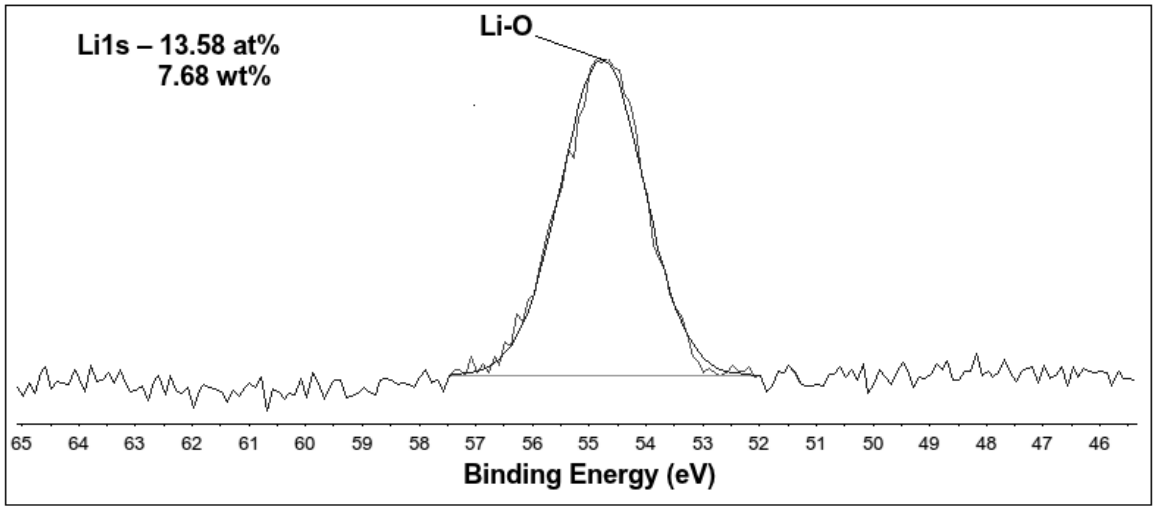

Figure 21: The Li 1s XPS spectrum of Lith-O-Graph shows that the material has only one Li environment

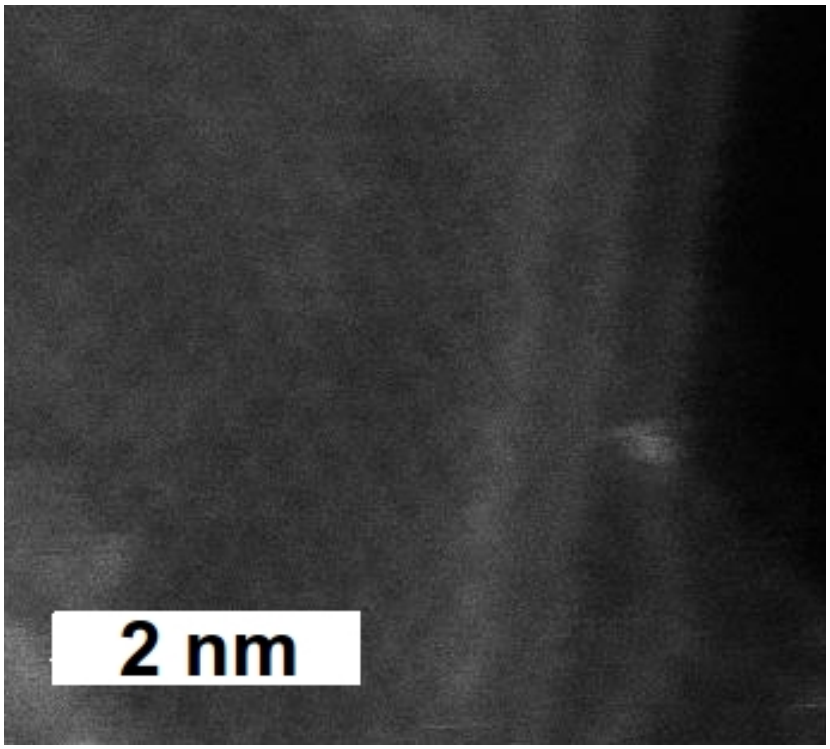

Figure 22: TEM image of TEGO, showing the edge of a TEGO nanoparticle comprised of three layers of stacked graphene sheets

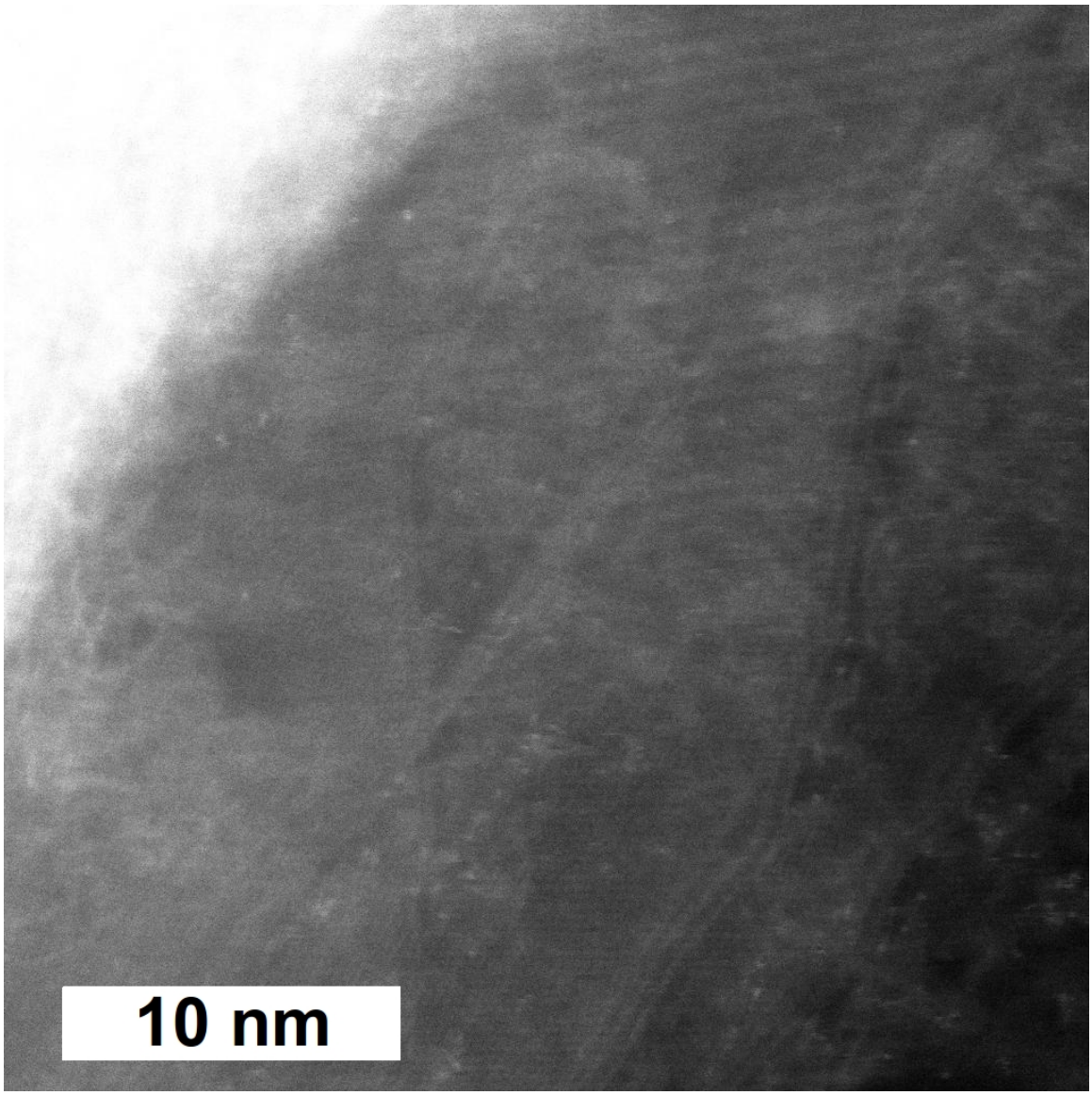

Figure 23: TEM image of several-layer thick TEGO, showing some heavier atoms adsorbed on the surface

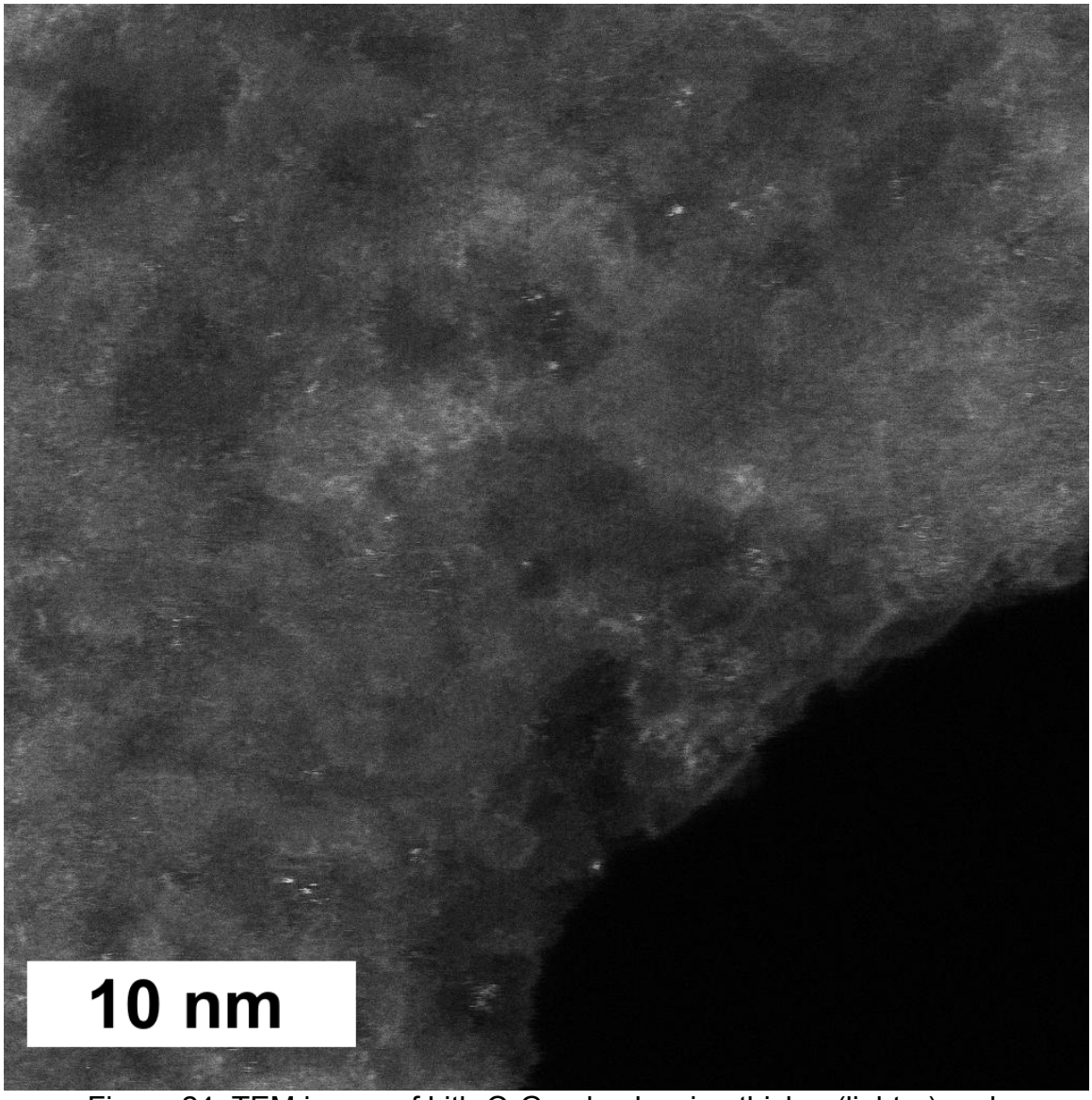

Figure 24: TEM image of Lith-O-Graph, showing thicker (lighter) and thinner (darker) areas within the particle

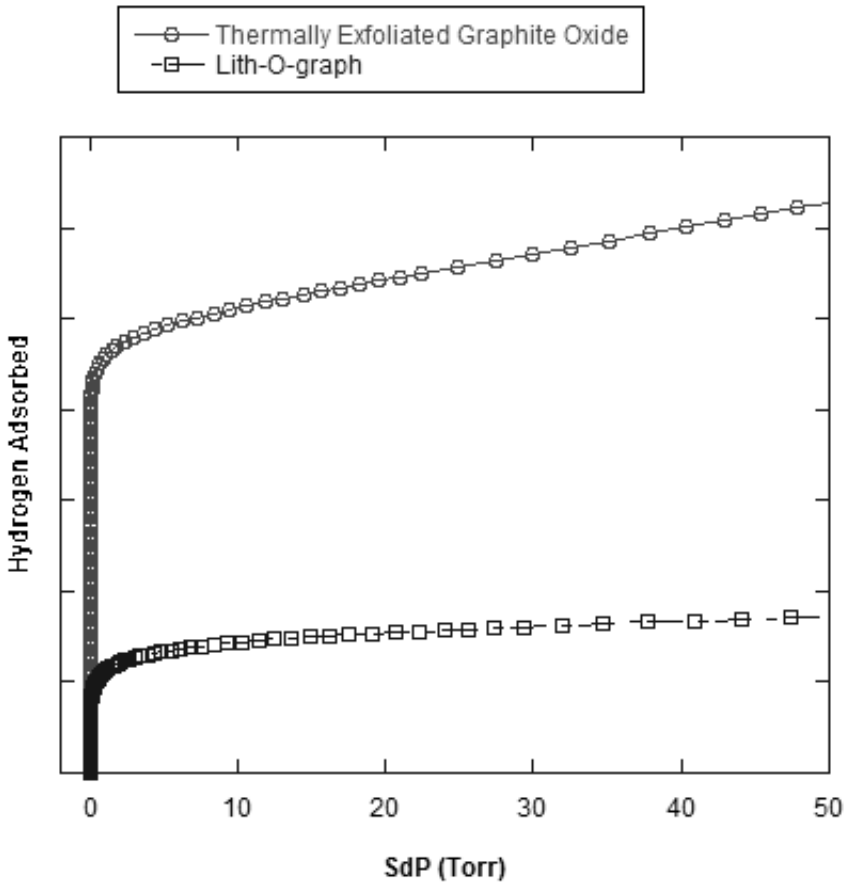

Figure 25: The hydrogen adsorption isotherm at 15 K shows that TEGO has more than 3X greater monolayer capacity

VITA

Benjamin Evan Estes was born in Hopkinsville, KY where he graduated from Christian County High School in 1995. He went on to obtain an Associate of Science Degree from Hopkinsville Community college in 2000 before completing a Bachelor of Arts Degree in Chemistry at Eastern Kentucky University in Richmond in 2002. While at Eastern Kentucky, Ben worked under the direction of C. Frank Shaw, III in the field of bioinorganic chemistry, modeling the sequestration of cadmium and mercury ions by the protein metallothionein.

Ben joined the research group of John F. C. Turner in the Department of Chemistry at the University of Tennessee during a summer undergraduate research assistantship in 2002, and entered the university as a graduate student in the fall of 2002. He studied organometallic synthesis and homogeneous catalysis for two and a half years before the group moved to Sussex University, England. Ben spent the next several years working for Genuine Parts Company as a management trainee and software implementation manager before returning to the University of Tennessee to work under the direction of John Z. Larese, also of the Department of Chemistry, in the fields of materials synthesis and heterogeneous catalysis. He completed his PhD in August 2012 in the field of Inorganic Chemistry.

Aside from his studies in the sciences, Ben has worked in commercial and industrial electricity and computer-controlled machine lathe assembly.